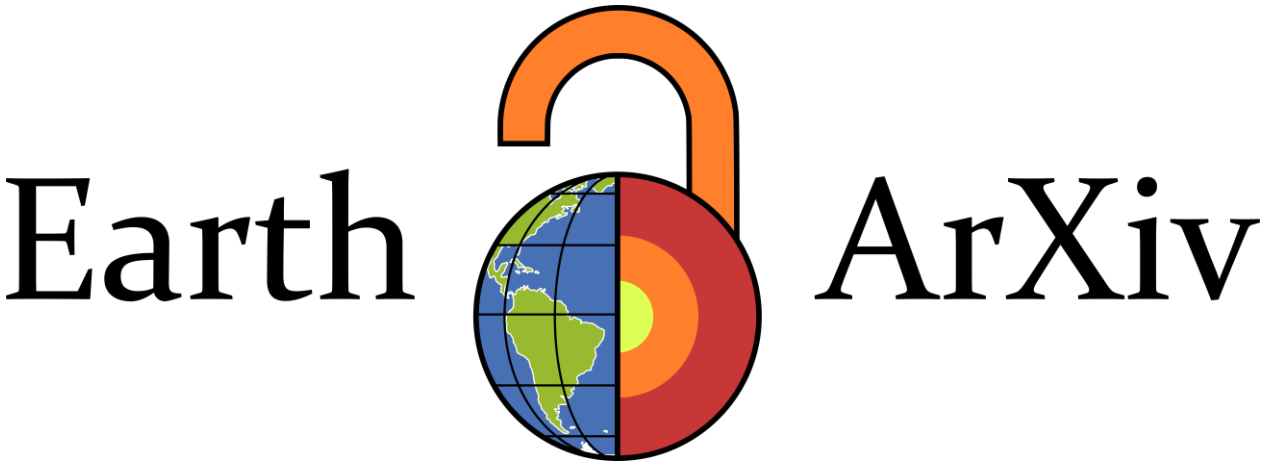

Title

Calcium promotes carbon rich grassland soils

Authors

Slessarev, E.W.,[1,2*] Goertzen, H.R.,[3] Lybrand, R.,[3] McFarlane, K.J.,[4] Pett-Ridge, J.[4,5,6], Sokol, N.[4], Zaharescu, D.[3] Georgiou, K.,[7]

Affiliations

[1] Department of Ecology and Evolutionary Biology, Yale University, New Haven, CT, USA
[2] Yale Center for Natural Carbon Capture, Yale University, New Haven, CT, USA[3] Department of Biological and Ecological Engineering, Oregon State University, Corvallis, OR, USA
[3] Department of Land Air and Water Resources, University of California, Davis, CA, USA
[4] Physical and Life Sciences Directorate, Lawrence Livermore National Laboratory, Livermore, CA, USA
[5] Innovative Genomics Institute, University of California Berkeley, Berkeley, CA.
[6] Life & Environmental Sciences Department, University of California Merced, Merced, CA.
[7] Department of Biological and Ecological Engineering, Oregon State University, Corvallis, OR, USA

*Corresponding author: eric.slessarev@yale.edu

Abstract

Dark colored grassland soils, known as Mollisols, are intensively farmed and exceptionally rich in organic matter, and hence have an important role in the carbon cycle. Elevated carbon storage in Mollisols may be facilitated by calcium (Ca) released by carbonate and silicate weathering. This synergy between carbon and Ca cycling has not been definitively quantified. To close this knowledge gap, we developed a novel geochemical model and leveraged continental-scale datasets to simulate Ca release in soils across the USA. We found that Ca released by mineral weathering helps to predict the distribution of Mollisols and soil organic carbon storage. Our model also indicates that agriculture has increased Ca inputs to cultivated USA Mollisols 2 to 5 fold, demonstrating that humans have fundamentally changed the geochemical conditions that sustain carbon storage in these soils. By implication, moderating the quantity of and timing of Ca release may be essential for sustaining soil carbon storage in the world's most intensively farmed landscapes.

Teaser

Calcium released by dissolving carbonate and silicate minerals helps to store organic carbon in Earth's most intensively farmed soils.

Introduction

Temperate grasslands feature exceptionally fertile, dark-colored soils known as Mollisols. Mollisols are the world's most intensively farmed soil type (*1*). Based on recent data (*2*, *3*), we estimate that Mollisols comprise only 7% of the Earth's land area yet support 24% of agricultural land and 32% of all calories from production of corn, soy, and wheat. Mollisols also contribute disproportionately to soil organic carbon storage, storing 32% of the organic carbon held in Earth's agricultural soils (see Materials and Methods). This makes Mollisols critical to land-based climate mitigation efforts. At the same time, Mollisols are exposed to environmental threats, including soil erosion (*4*), and have lost a significant fraction of their carbon to cultivation (*5*). Effective stewardship of Mollisols in the face of these threats requires a comprehensive understanding of the environmental factors that make them fertile and carbon rich.

There are several ecological processes that contribute to the carbon richness of Mollisols, and these have implications for protecting and restoring soil organic carbon. As early as the 1860's, grassland vegetation was identified as the main driver of Mollisol formation (*6*). Perennial grasses grow extensive fibrous root systems, and root turnover is an important pathway of soil organic carbon accrual (*7*, *8*). Grasslands and savannas are characterized by frequent fires, and fires can generate persistent pyrogenic carbon that might explain the origin of Mollisols (*9*). Grasslands also support robust populations of burrowing animals that contribute to the thick, carbon-rich topsoil layers characteristic of Mollisols (*10*). Contemporary proposals for restoring carbon storage in cropland soils mimic ecological processes that are thought to be important in Mollisols; for instance, carbon sequestration might be achieved by returning deep rooted cultivars to croplands (*11*), increasing plant diversity (*12*), or amending soils with pyrogenic carbon (*13*),

Geologic factors can also help to explain the origins of Mollisols. Mollisols are commonly formed from calcareous rocks or from aeolian deposits rich in calcium carbonate (*6*). A growing body of evidence shows that Ca stabilizes soil organic matter. Ca facilitates sorption of organic molecules on clays and promotes the growth of bacterial biofilms that are retained on mineral surfaces (*14*–*16*). These processes manifest at continental scales, where soil organic carbon is spatially correlated with exchangeable Ca^{2+}, i.e., Ca^{2+} that is reversibly bound to surfaces (*17*, *18*). The relative abundance of exchangeable Ca^{2+} and other base cations (Mg^{2+}, K^{+}, and Na^{+}) is important in classifying Mollisols, reflecting their role in Mollisol genesis (*19*). These facts suggest that judicious management of soil Ca might also be a tool to promote organic carbon storage, although this possibility has received relatively scant attention. This is in part because the availability of Ca^{2+} in soil is a function of complex interactions among vegetation, geology, and climate. This makes it challenging to disentangle the role of Ca from other drivers of carbon storage in Mollisols.

We addressed the role of Ca in Mollisol organic carbon storage by developing and applying a novel geochemical model across the conterminous USA. Our modeling approach leveraged soil mineralogy data available across the USA (*20*), which enabled us to represent soil chemical processes at an unprecedented spatial extent. We designed our model to track the inputs and outputs of major cations and anions to the soil solution, allowing us to simulate soil pH, mineral weathering rates, and associated Ca release and retention. We used the model to quantify specific Ca sources: carbonate weathering, silicate weathering, and atmospheric deposition. We then statistically estimated the effect of each source on Mollisol extent and carbon storage while accounting for vegetation and climate. Using this approach, we isolated the effect of specific geologic Ca sources on Mollisols and quantified the role of Ca in sustaining Mollisol organic carbon stocks.

Results and Discussion

Geochemical model performance

We used our geochemical model to estimate the input of available Ca to soil across the conterminous USA and then related Ca inputs to: [1] Mollisol extent, derived from ground based soil classification and mapping (*21*) (Fig. 1a); and [2] observations of topsoil (A-horizon) organic carbon stocks (*22*, *23*) (Fig. 1b). We first parametrized the model with input data including climate, atmospheric deposition of major solutes, net primary productivity, agricultural element budgets, and soil mineralogy (see Methods). The model integrated these variables by linking inputs and outputs of solutes, the release of CO_2 and organic acids by biota, and mineral weathering via a set of pH-dependent equilibrium reactions. We calibrated two unconstrained parameters related to mineral surface reactivity, training the model to match modern observations of soil pH. The model performed relatively well, explaining 69% of the spatial variation in depth-averaged soil pH (0-100 cm), 39% of the variation in soil exchangeable Ca^{2+}, and 64% of the variation across all exchangeable ions when applied to a separate validation set of ground observations (Fig. S1, Fig. S2, Table S1). We re-parametrized the model to reflect preindustrial (1850) rates of atmospheric deposition (*24*) and eliminated agricultural processes following calibration and validation steps. We then simulated Ca release from carbonate and silicate weathering and exchangeable Ca^{2+} under pre-industrial conditions.

Environmental controls on Mollisols

Our geochemical model shows that Mollisol extent correlates with the inputs of available Ca (Fig. 1c) and also with the presence of grassland vegetation (Fig. 1d). To disentangle these correlations, we applied a multivariate logistic regression, quantifying the present-day influence of Ca on the geographic distribution of Mollisols while accounting for vegetation and other climate and soil factors. We used the base saturation percentage to represent the influence of Ca in the regression because this index is one of several factors used to classify and map Mollisols in the USA (*19*) [base saturation = 100*(total base cation charge / cation exchange capacity)]. We also included six additional factors: [1] the pre-agricultural grassland and savanna distribution, which we approximated with a potential vegetation map derived from remotely sensed patches of relict vegetation (*25*); [2] mean annual temperature; [3] mean annual precipitation; [4] soil silt and clay content [5] soil drainage class; [6] net primary productivity. We compared the independent explanatory power of these factors by computing scaled regression coefficients (Table S2). The regression model matched the observations relatively well, classifying 79% of locations correctly. We found that base saturation was the strongest predictor of the distribution of Mollisols, followed by grassland and savanna presence, mean annual air temperature, precipitation, and other soil properties (Fig. 2a). Together, these results indicate that Mollisols are associated with grassland environments rich in Ca^{2+} and other base cations, particularly in drier and cooler climates.

Our results indicate that base cations, including Ca^{2+}, are an important control on the distribution of Mollisols. However, these results are not direct evidence that Ca enhances Mollisol organic carbon storage; rather, they show that the relative abundance of exchangeable Ca^{2+} and other base cations strongly influences where Mollisols are mapped. To address the role of Ca in organic carbon storage directly, we related modeled exchangeable Ca^{2+} to soil carbon stock data retrieved from two databases, the US Department of Agriculture Rapid Carbon Assessment and the National Cooperative Soil Survey archives (*22*, *23*). We used these data to quantify A-horizon organic carbon stocks across the USA (Fig. 1b). Mollisols are characterized by thick, carbon-rich A-horizons (*19*); hence we used total A-horizon carbon—incorporating both topsoil thickness and carbon content—to quantify the primary mode of carbon storage in Mollisols.

We related A-horizon organic carbon stocks to total exchangeable Ca^{2+} using multiple linear regression. We also included the same set of variables used for interpreting Mollisol extent, plus

the sum of non-Ca exchangeable cations (Mg^{2+}, K^{+}, Na^{+}, Al^{3+}, and H^{+}). The regression model explained 30% of the variation in A-horizon organic carbon stocks. Comparison of the scaled regression coefficients revealed that net primary productivity and temperature were the most important predictors of A-horizon carbon storage, followed by exchangeable Ca^{2+}, the presence of grasslands or savannas, and then other factors (Fig. 2b; Table S3). The controls on A-horizon carbon storage across the conterminous USA are distinct from the controls on Mollisol extent because Mollisols are not the only soil types that feature carbon-rich topsoil. For instance, cool, productive forests in the northwestern USA accumulate soil organic carbon due to high organic matter inputs, inhibition of decomposition by low temperatures, and abundant reactive Al and Fe minerals (*26*). It is nonetheless clear that exchangeable Ca^{2+} is an important secondary control on A-horizon carbon storage. Furthermore, the combined effect of other exchangeable ions was weak, suggesting that it is specifically Ca, rather than total cation exchange capacity, that contributes to A-horizon carbon storage.

Our regression analysis identifies a major role for Ca in Mollisol function, but also suggests that grassland and savanna vegetation influence the distribution of Mollisols independent of other factors. Grasslands and savannas can be maintained by fire, helping grasses to persist in climates that would otherwise support forest (*27*, *28*). In this case, fire regimes that maintain grass dominance might directly determine where Mollisols form. On the other hand, Mollisols are notably uncommon in tropical grasslands and savannas (*29*), which suggests that ecological factors common to grasslands and savannas are not sufficient to generate Mollisols. Tropical soils are typically highly weathered, host less reactive minerals, and are generally more acidic than temperate soils that received Ca-rich minerals following Pleistocene glaciation (*30*, *31*). These geologic limits to Ca supply, in addition to climate, may curtail Mollisol development in the tropics. By contrast, multiple overlapping environmental factors—including Ca weathering in post-glacial soils, cooler temperatures, mesic climate, and the presence of grasses—converge in certain temperate regions, and Mollisols are an emergent result of these overlapping factors.

Geologic drivers of Mollisol carbon storage

Our geochemical model enabled us to consider the specific geologic mechanisms that explain the distribution of Mollisols. We evaluated the effect of Ca sources on Mollisol extent by constructing counterfactual scenarios in which Ca sources were suppressed under simulated preindustrial conditions. Specifically, we [1] set carbonate weathering, all silicate weathering, or atmospheric Ca deposition to zero in the geochemical model, [2] used updated outputs from the geochemical model to generate predictions using the previously fitted logistic regression, and [3] quantified changes in the predicted area of Mollisols. For reference, we also created a counterfactual scenario in which all vegetation was assumed to be non-grassland. This analysis revealed that both carbonate and silicate weathering help to explain the presence of Mollisols. In the absence of carbonate weathering, predicted preindustrial Mollisol extent was 4% lower (4 Mha), and without silicate weathering Mollisol extent was 27% lower (52 Mha). When both weathering sources were eliminated, the effect was non-additive: Mollisol extent dropped by 90% (174 Mha), which was comparable to the effect of eliminating grassland vegetation (85%, 166 Mha). By contrast, eliminating atmospheric Ca deposition reduced Mollisol extent by only 2% (4 Mha) (Fig. 3a).

We also evaluated the effects of specific geologic Ca sources on A-horizon organic carbon by eliminating Ca sources in the geochemical model as above. This analysis indicated that carbonate and silicate weathering jointly promote A-horizon soil organic carbon storage. Across the conterminous USA, predicted preindustrial A-horizon carbon storage was 5% (1.2 Pg C) lower when carbonate weathering was eliminated, 2% (0.6 Pg C) lower when silicate weathering was eliminated, and 11% (2.9 Pg C) lower when both were eliminated together (Fig. 3b). This combined effect was similar to eliminating grassland vegetation, which reduced A-horizon organic carbon

storage by 10% (2.7 Pg C) (Fig. 3b). When we focused our analysis on Mollisol regions, we found A-horizon organic carbon stocks were even more sensitive to eliminating carbonate and silicate weathering (16% reduction, 1.2 Pg C) and grassland vegetation (19%, 1.5 Pg C).

Taken together, our results show that carbonate weathering and silicate weathering have modest effects on Mollisol extent and A-horizon carbon storage when considered alone, but a more substantial effect when combined at a continental scale. This result emerges because carbonate weathering and silicate weathering suppress each other via their alkalizing effect on soil pH; hence eliminating one Ca source yields a compensatory increase in Ca release from the other. Consequently, when either silicates or carbonates are sufficiently abundant, soil Ca^{2+} availability is high and Ca^{2+} generally predominates over other exchangeable ions. These conditions favor Mollisol formation and organic carbon accrual across a range of geologic settings.

Our model suggests that the elevated Ca inputs that generate Mollisols in the midcontinental USA are derived from specific geologic sources, particularly carbonate minerals (Fig. 3b). Glacial deposition explains elevated carbonate weathering in the north-central USA, where lobes of the Laurentide ice sheet ground up and distributed underlying limestone and dolomite rocks during the last ice age (*32*). Farther south, soil carbonates are abundant in the aeolian Bignell Loess deposits (*33*). and in the predominately limestone rocks of the Edwards Plateau (*34*), both of which support Mollisols. Carbonate minerals are also abundant in the arid Western USA; however, our geochemical model predicts that carbonates are either a minor source or a Ca sink in this region (Fig. S3). While some of the carbonates in these soils may be derived from sedimentary rocks, desert carbonates are often primarily derived from in-situ precipitation of $CaCO_3$ from aeolian Ca (*35*). Our model suggests that some of these carbonates may be slowly weathering under late-Holocene conditions, supplying Ca to overlying Mollisols.

Our model also predicts that inputs of Ca from deposition are significant in much of the USA (Fig. 3c); however, we found that atmospheric deposition of Ca is a minor control on Mollisol extent (Fig. 3a). We assumed that preindustrial Ca deposition was five-fold lower in North America than at present based on paleo dust records (*36*). Dust fluxes in the midcontinental USA were substantially higher in the late Pleistocene than in recent preindustrial times due to glaciation (*37*). Ca in modern soil carbonates is often inherited from Pleistocene dust (*38*), and carbonates continue to weather in Pleistocene loess deposits. Thus, over geologic timescales, atmospheric Ca deposition during glacial periods may set the stage for future carbonate weathering, helping to build Mollisol organic carbon stocks.

Implications for Mollisol conservation and climate mitigation

Our results imply that changes in soil Ca inputs due to cultivation might affect organic carbon cycling in Mollisols. To address this possibility, we used our model to evaluate the magnitude of changes to the Ca balance of Mollisol croplands relative to preindustrial conditions. We parametrized the model with modern day atmospheric deposition chemistry, enabled agricultural fertilizer addition and nutrient removal, and estimated agricultural liming rates. This analysis shows that soil Ca cycling has changed dramatically in two ways (Fig. 4). First, the model predicts that acid inputs from fertilizer and atmospheric deposition have accelerated Ca release from carbonate weathering by 23% (± 20%) in Mollisols. Second, agricultural liming has massively increased Ca inputs to cropland soils (Fig. 4). Taking modeled liming rates as a reference point, agriculture has more than doubled Ca inputs to Mollisol cropland soils and increased Ca input to non-Mollisol cropland soils by 9-fold relative to preindustrial levels. Alternatively, we can take the most recent available agricultural census liming data (*39*), which are from 1987, as a reference point. We estimate that agriculture has increased Ca inputs to Mollisol cropland soils by 5-fold and non-Mollisol cropland soils by 16-fold based on 1987 liming rates assuming that lime is 20% dolomite and 80% calcite (*40*).

Clearly humans have dramatically altered the Ca cycle, and this has the potential to alter carbon storage in Mollisols. Our finding that agriculture has accelerated dissolution of native carbonates is consistent with other studies that have linked agricultural soil acidification to soil inorganic carbon loss, although the acceleration of carbonate weathering predicted by our model is modest compared to estimates in highly acidified systems (e.g., in China) (*41–43*). Our simulations indicate that the more significant perturbation to the soil Ca cycle is agricultural lime addition. Adoption of enhanced silicate (*44*) or carbonate (*45*) weathering for carbon dioxide removal will further perturb the Ca cycle. These practices increase soil Ca inputs, which we have shown contribute to Mollisol organic carbon storage over geologic timescales. However, increased Ca inputs have occurred in response to unprecedented acid addition to cropland soils, and the effects of these competing processes are hard to predict. For instance, experimental studies have found that the effect of agricultural liming on soil organic carbon is not necessarily positive in the short term (*46*). Similarly, enhanced silicate weathering does not necessarily benefit soil organic carbon storage in the short term (*47*). Liming may affect soil carbon differently than natural weathering because it is intermittent: in the USA only 5-20% of cropland is limed in any given year (*48*). Variable Ca availability caused by intermittent liming may alternately stimulate and suppress decomposition, with net effects that are challenging to predict.

In the broader context of conservation agriculture, our results suggest that farming practices that mimic pre-agricultural vegetation in grasslands by increasing root inputs, increasing plant diversity, or reducing tillage may not be sufficient to preserve Mollisol carbon. Instead, vegetation-focused strategies may need to be complimented with geochemical strategies that mimic the natural Ca cycle of these soils. For instance, reducing excess N can protect soil carbonates, which reduces emissions from dissolution of soil inorganic carbon by strong acids (*43*), while also preserving a critical Ca reservoir that helps to protect soil organic carbon. In addition, changing the cadence and quantity of lime applied to croplands could better simulate the natural weathering regime. These efforts must be supported by collection of baseline statistics on the agricultural Ca budget, which remains poorly quantified (*48*). Closing these knowledge gaps is critical to managing Earth's most fertile soils sustainably.

Materials and Methods

Quantifying global role of Mollisols

We calculated the total land area of Mollisols, the fraction of global agricultural production occurring on Mollisols, and the fraction of agricultural soil organic carbon stored by Mollisols using the Harmonized World Soil Database, Version 2.0 (HWSD) (*2*). For this analysis we assumed that the distribution of Mollisols can be approximated by aggregating three World Reference Base soil groups: Chernozems, Phaeozems, and Kastanozems (*49*). HWSD soil mapping units were assigned values based on the dominant soil type in each unit. Organic carbon storage in croplands and Mollisols was calculated from the HWSD and summed to 1 m depth. We then combined the HWSD with the 1 km resolution GFSAD 2010 croplands mask (*3*) to estimate the area of croplands and cropland organic carbon storage. Production of wheat, corn, and soy occurring on Mollisols was obtained by combining the HWSD with SPAM global production maps for 2010 (*50*). Production values were rescaled to calories based on UN Food and Agriculture Organization Annex I food composition tables (*51*).

Geochemical model overview

We developed a simplified geochemical model to simulate the release of Ca from silicate and carbonate weathering in the top 1 m of soil across the USA. We parametrized the model with existing data when possible and then calibrated remaining parameters related to mineral surface reactivity so that modeled soil pH matched observed modern soil pH across the study region. We based our model on existing geochemical models that were designed to simulate soil acid-base chemistry in response to acid rain (*52*). Our model also incidentally resembles approaches used to simulate enhanced silicate weathering (*53*). although it was not designed for this purpose and is less complex. The model treated the entire upper 100 cm of soil as a single chemically homogeneous reservoir, tracking the inputs and outputs of seven ions that control soil pH and weathering rates: Ca^{2+}, Mg^{2+}, Na^{+}, K^{+}, SO_4^{2-}, NO_3^{-}, Cl^{-}. These ions were sourced from dissolution of silicate and carbonate minerals, atmospheric deposition, agricultural inputs, and biological fixation in the case of N. Ions were lost via leaching, carbonate mineral precipitation, export in crop biomass, and volatilization in the case of N. Additional ions were assumed to equilibrate instantaneously with the soil solution and hence were modeled implicitly as a function of other factors: H^{+}, Al^{3+}, $Al(OH)^{2+}$, $Al(OH)_2^{+}$, AlH_2Org^{2+}, $AlHOrg^{+}$, OH^{-}, CO_3^{-}, HCO_3^{-}, H_2Org^{-}, $HOrg^{2-}$, Org^{3-}, $Al(OH)_4^{-}$. We approximated ion activities with concentrations because under most conditions modeled ionic strengths were too low to affect our results. Mineral concentrations were treated as constant at the timescales being modeled. While the model was able to simulate year-to-year weathering dynamics, for the purposes of this analysis, we applied a steady-state solution because this simplified computations substantially. The model had nine governing equations: one for each of the seven conserved ions and two algebraic constraints stipulating charge balance and conservation of ions adsorbed on the soil exchange complex (Table S4). A full description of the model is provided in the Supplementary Materials file.

Input data

Whenever possible, we used spatially explicit environmental data to assign model parameters. When applicable, we used time-averaged environmental parameters to drive the model, setting the years 2001-2010 as our reference period for recent environmental conditions. To capture pre-industrial conditions, we reset deposition rates for N and S, reset atmospheric pCO_2, and turned off the model's agricultural nutrient budget.

To parametrize climate and soil hydrologic properties, we used several sources. We derived mean annual air temperature from PRISM 30-year normals (1991-2020) at an 800 m resolution (*54*) and treated air temperature as a proxy for soil temperature when running the model. We calculated

recharge (RC) using the Global Streamflow Characteristics Database (GSCD), which provides 0.125 degree resolution estimates of streamflow and base flow index (*55*). We calculated recharge by multiplying streamflow by the baseflow index. We constrained soil moisture with the satellite-informed Global Land Evaporation Amsterdam Model (GLEAM) V3.8 root zone soil moisture dataset (0.25 degree resolution) (*56*). We also obtained pedotransfer-based maps of wilting point and field capacity from GLEAM. Finally, we parametrized net primary productivity (NPP) using MOD17 (500 m resolution) (*57*).

We parametrized soil mineralogy using two sources. For silicate minerals, we spatially interpolated data from the North American Soil Geochemical Landscapes Project (NASGLP) (*20*), which includes estimates of major element abundance and quantitative X-ray diffraction data for a selection of silicate and carbonate minerals. We used these data to directly constrain some minerals and approximate concentrations of others that are not directly reported by NASGLP. First, we averaged A-horizon and C-horizon data at the NASGLP sampling locations. We then interpolated the NASGLP data for each mineral to locations where we ran the geochemical model, using inverse distance weighting with an exponent of 2 and an averaging neighborhood of 75 km. Plagioclase feldspar and the plagioclase anorthite fraction (fAn) were estimated by first multiplying the molar concentration of Na from the NASGLP by the formula weight of albite. Where albite exceeded 80% of the total plagioclase feldspar content obtained from the NASGLP, albite was reset to 80% of the plagioclase content. Anorthite was then assumed to make up the remainder of the plagioclase pool (*26*). K-feldspar, hornblende, and pyroxene were taken directly from the NASGLP X-ray diffraction estimates. To represent clay minerals, we limited our analysis to chlorite (clinochlore) and illite (approximated as muscovite), which we treated as generalized categories that stand in for the full diversity of Mg- and K-bearing 2:1 phyllosilicates (e.g. vermiculite and smectite group clays). Illite was calculated by subtracting the K in K-feldspar from total K and assigning all residual K to illite. Similarly, chlorite was calculated by first calculating the amount of Mg in hornblende, pyroxene, and dolomite (Table S6). This value was subtracted from total Mg, and any residual Mg was assigned to chlorite.

To estimate carbonate mineral stocks, we did not use NASGLP data directly. Given the high weatherability of carbonates, small quantities of carbonate mineral had a large effect on modeled soil pH values; hence we used high-resolution digital soil maps from NATSGO (*21*) to ensure accurate assignment of soil carbonate content. We first calculated the stock of carbonate in $CaCO_3$ equivalents to 1 meter depth from NATSGO. Next, we subdivided this stock into calcite and dolomite components by using the data from the NASGLP to calculate the ratio of calcite to dolomite. In addition to $CaCO_3$ content, we derived soil texture (silt, sand, and clay percentages), cation exchange capacity, and soil bulk density parameters from NATSGO, averaging these properties over the top 1 meter of soil or to bedrock if shallower than 1 meter. All NATSGO soil properties were summarized by calculating the share-weighted average within soil mapping units. Data were then extracted using the 30-meter resolution gridded version of NATSGO.

We parametrized the cropland N inputs and outputs using a county-level nutrient budget for the period 1987-2012 (*58*). We ran the geochemical model in one of two modes, either with cropland nutrient imports and exports enabled or with only natural N fixation rates enabled. We determine which mode to use by assigned modeled locations to cropland or non-cropland land cover using the GFSAD 1 km cropland mask (*3*).

We parameterized deposition of N, S, Cl, Ca, Mg, Na, and K, using gridded data from the US Environmental Protection Agency's National Trend Network (*59*), which we averaged for 2001-2010. To represent preindustrial deposition of N and S, we used the multi-model average from the ACCMIP project for the year 1850 (*24*). For Cl, Ca, Mg, Na, and K no data from before the year 2000 were available. Human activity has increased deposition of base cations, including Ca, in the

Western USA (*36*). To account for this trend, we applied a factor of 5 difference between recent and preindustrial times, which approximates dynamics recorded in lake sediment cores in Colorado (*36*). We applied this multiplier to Ca, Mg, and K, but left Na unchanged since this solute is primarily derived from marine aerosols outside of deserts.

Model calibration and uncertainty

We implemented the model at point locations, extracting data from the aforementioned environmental datasets at each point. For the calibration and validation steps, we selected points by acquiring soil pH data from the USDA NRCS National Cooperative Soil Survey (NCSS) Kellogg Soil Survey Laboratory database. We computed depth weighted average pH values in a 1:1 water matrix for all soil profiles with available data to a depth of 1 m, or to the depth of the lowermost C horizon in cases where the profile terminated below 1 m. Similarly, we computed depth-weighted average values for exchangeable cations using the NCSS database. We represented Ca^{2+}, Mg^{2+}, Na^{+}, and K^{+} using NH_4-acetate (pH 7) extraction data and Al^{3+} from KCl extraction. Exchangeable H^{+} was estimated by subtracting the sum of exchangeable Ca^{2+}, Mg^{2+}, Na^{+}, K^{+}, and Al^{3+} from the cation exchange capacity (CEC) obtained by the NH_4-acetate method. When the sum of these ions exceeded the CEC, exchangeable H^{+} was set to zero and the values of all ions were rescaled by the value (CEC / sum cations) so that the sum equaled the CEC.

We spatially resampled the pH and exchangeable cation data by binning them into 1 degree by 1 degree cells based on their latitude and longitude and then resampling 6,000 locations with replacement, with sampling weights inversely proportional to the number of profiles in each cell. We extracted environmental data at these points and discarded those with missing data, yielding 4,149 unique pH observations that were evenly distributed across the conterminous USA (Fig. S1). Exchangeable ions were only reported at 2,484 locations with pH measurements. Because we resampled with replacement, some soil profiles occurred more than once by design; the total number of pH observations was 5,389 (including pseudo-replicates) and the total number of exchangeable cation observations was 3,280.

We calibrated the model by randomly sampling 2,000 training points from the NCSS profiles and using them for model inversion based on soil pH. We optimized two parameters, r_2 and r_3, which controlled the reactivity for secondary phyllosilicate minerals and carbonate minerals respectively (see Supplementary Materials). We calibrated the model using a Markov Chain Monte Carlo (MCMC) approach, applying the adaptive Metropolis Hastings algorithm with delayed rejection (*60*) implemented via the R package FME (*61*). The cost function was defined to minimize errors in soil pH. We initiated the MCMC algorithm with manually calibrated initial parameter values and uninformative priors. The initial model variance was set equal to the mean squared residuals based on the initial parameter estimates, and the initial jump values were set to 10% of the initial parameters. The adaptive stage of the algorithm was run for a burn-in period of 1,000 iterations updating the covariance matrix every 50 iterations with the number of delayed rejections steps set to 2. After burn-in sampling continued for an additional 1,000 iterations. We checked for convergence by running the algorithm using perturbed values of the starting parameters and different training samples and found that results were comparable. The final calibration yielded values of $10^{-6.8}$ for r_2 and $10^{-6.3}$ for r_3.

We estimated uncertainty in modeled Ca fluxes using a Monte Carlo approach. We expanded this analysis beyond the calibrated parameters to address uncertainty in all parameters, excepting chemical formulae and well-known physical constants. Variables and parameters included in the uncertainty analysis included: soil moisture, field capacity, wilting point, recharge, net primary productivity, temperature, all deposition fluxes, all components of the agricultural N budget, cation exchange capacity, sand, silt and clay fractions, bulk density, the reaction order for silicate weathering, all mineral surface areas, all constants related to organic acid equilibria, Q_{10}, decay

rate, and input rate for DOC, the coefficient for gaseous loss of N, weathering rate parameters r_1, r_2,and r_3, and all cation exchange constants. Uncertainties for most of these parameters could not be constrained. Instead, we applied a uniform relative uncertainty distribution of +/- 20% to each variable or parameter. Specifically, we ran the model at the 2,000 calibration points 1,000 times, randomly rescaling each parameter or environmental input by a value between 80% and 120% of the observed value. We treated the standard deviation of the Ca flux distributions derived from this process as a first-order estimate of uncertainty given an assumed 20% range in all inputs.

Statistical analysis

After calibrating the geochemical model, we used it to create maps of preindustrial Ca pools and fluxes across the conterminous USA. We used these maps to quantify the strength of the relationships between occurrence of Mollisols, A-horizon organic carbon, and soil Ca availability using logistic regression. To create the maps, we established a 10-kilometer resolution grid across the study region and extracted environmental data at each point in the grid. Presence or absence of Mollisols was obtained from NATSGO. For each NATSGO map unit, we identified the soil order with the largest share (areal contribution), excluding non-soil land classes. When modelling Mollisol extent, we represented soil Ca availability with the modern base saturation percentage. Predicted Mollisol extents were obtained by applying a probability threshold to the logistic regression output, with the threshold optimized so that predicted Mollisols land area equaled the actual mapped area (probability = 0.4).

Following a similar protocol, we quantified the strength of the relationship between A-horizon soil organic carbon (SOC) stocks from RaCA (*22*) and the NCSS (*23*) databases and Ca using ordinary least squares regression. When working with data from RaCA and NCSS, we calculated the SOC stock in all horizons with the master designation "A". The SOC stock (kg C m^{-2}) was calculated from the organic carbon percentage (OC%), the inorganic carbon percentage (IC%), A-horizon thickness (TH, cm), rock fraction (RF, unitless) and bulk density (BD, g cm^{-3}) as:

$$SOCstock = ((OC\% - IC\%)/100)*BD*TH*(1-RF)*10 \qquad \text{(Equation 23)}$$

Inorganic carbon was calculated from $CaCO_3$ equivalents reported in RaCA. In the few cases where IC% exceeded OC%, OC% was set to zero. In the case of NCSS, we used the "estimated organic C" field, which is already corrected for IC where applicable, or organic carbon content estimated via the Walkley Black method when this field was not available. After calculating SOC in each A horizon, we summed all A horizon stocks for each pedon to obtain total A-horizon SOC. We log transformed A-horizon SOC stocks before fitting the model. When modelling A-horizon SOC, we used modern total exchangeable calcium (ceq kg^{-1}), and also included the sum of all other exchange ions as an additional predictor in the regression model.

In specifying both regression models, we included the presence of grassland vegetation as a predictor using potential natural vegetation maps developed by ISCLP. We treated grassland presence as a binary predictor, combining grasslands and savannas into a single category (present = 1, absent = 0). In addition to vegetation, we controlled for mean annual temperature and mean annual precipitation based on 30-year normals from Prism (*54*). We also included three additional potential confounding variables: the logarithm of average NPP, derived from MOD17 for the period 2001-2010, average silt plus clay content of the top meter of soil, and soil drainage class. The latter two variables were derived from NATSGO (*21*). Drainage class categories were assigned numerical values from 1-7, with 1 being excessively drained and 7 being very poorly drained. When fitting the regression model for SOC, we also included the sum of non-Ca exchangeable ions (ceq kg^{-1}) as an additional predictor. We compared the relative importance of different predictors in the regression models by standardizing all predictors upstream of fitting the

models. We standardized by dividing predictors by two times the standard deviation, which is recommended in cases when some predictors are binary (*62*).

In addition to computing scaled coefficients, we evaluated the effect of specific Ca sources on Mollisol extent and A-horizon SOC under preindustrial conditions. We evaluated the effect of cation inputs from carbonate weathering and silicate weathering by running the model with each mineral cation source eliminated, which meant that Ca, but also Mg, K, and Na fluxes were affected by removing each source. We achieved this by re-setting the surface areas of all silicates, all carbonates, or both mineral types to zero. In the case of deposition, we set base cation deposition to zero. Each of these modified model runs generated predictions of exchangeable Ca in the absence of each cation source; these values were then used as inputs to the fitted regression models and used to predict either Mollisol extent or A-horizon SOC. We also quantified the effect of eliminating grasslands by setting the ISCLP-derived grassland and savanna predictor to zero everywhere and then obtaining predictions from the fitted regression models.

We ran regressions on the full population of model evaluation points (n = 77,115 points sampled from NATSGO; 11,332 A-horizon SOC estimates from RaCA and NCSS). We addressed the spatial dependence of these observations by performing nonparametric spatially blocked bootstrapping (*26*). This involved dividing the data (NATSGO grid or RaCA/NCSS based) into blocks defined by 2-by-2 degree grid cells and then resampling the cells with replacement 1,000 times. We fit a logistic or ordinary least squares regression to each of the 1,000 resampled datasets and stored the regression coefficients. We then calculated bias corrected and accelerated 95% confidence intervals from the bootstrap replicates (*63*). We followed the same protocol for estimating uncertainty associated with predicted Mollisol areas and A-horizon SOC stocks after resetting the model inputs as described above.

Soil organic matter can contribute to cation exchange capacity, which may explain a relationship between total exchangeable calcium and SOC even in the absence of an effect of Ca on SOC persistence. To account for this possibility, we conducted an additional regression analysis after correcting total cation exchange capacity for the contribution of soil organic matter. Corrected cation exchange capacity (CEC-c, ceq kg^{-1}) was obtained from the uncorrected CEC and the soil organic matter percentage (SOM%) from NATSGO:

$$\text{CEC-c} = \text{CEC} - \text{CEC-OM}*(\text{SOM\%}/100) \qquad \text{(Equation 24)}$$

Where CEC-OM is the cation exchange capacity of organic matter, assumed equal to 200 ceq kg^{-1} (*64*). This formula could generate negative or zero values, and so in cases where CEC-c was less than a minimum value of 0.01 we re-set it to this value. The results of the regressions computed with CEC-c were similar to the primary results (Fig. S5).

References

1. X. Liu, C. Lee Burras, Y. S. Kravchenko, A. Duran, T. Huffman, H. Morras, G. Studdert, X. Zhang, R. M. Cruse, X. Yuan, Overview of Mollisols in the world: Distribution, land use and management. *Can. J. Soil. Sci.* **92**, 383–402 (2012).

2. *Harmonized World Soil Database Version 2.0* (FAO; International Institute for Applied Systems Analysis (IIASA);, 2023; http://www.fao.org/documents/card/en/c/cc3823en).

3. P. Teluguntla, P. Thenkabail, J. Xiong, M. Gumma, C. Giri, C. Milesi, M. Ozdogan, R. Congalton, J. Tilton, T. Sankey, R. Massey, A. Phalke, K. Yadav, NASA Making Earth System Data Records for Use in Research Environments (MEaSUREs) Global Food Security Support Analysis Data (GFSAD) Crop Mask 2010 Global 1 km V001, NASA Land Processes Distributed Active Archive Center (2016); https://doi.org/10.5067/MEASURES/GFSAD/GFSAD1KCM.001.

4. E. A. Thaler, I. J. Larsen, Q. Yu, The extent of soil loss across the US Corn Belt. *Proc. Natl. Acad. Sci. U.S.A.* **118**, e1922375118 (2021).

5. B. Boincean, D. Dent, "Potential of Chernozem to Increase Food Security and Mitigate Global Warming" in *Farming the Black Earth* (Springer International Publishing, Cham, 2019; https://link.springer.com/10.1007/978-3-030-22533-9_8), pp. 189–204.

6. V. V. Dokuchaev, *The Russian Chernozem* (1883)*US Department of Agriculture Israel Program for Scientific Translations*.

7. D. P. Rasse, C. Rumpel, M.-F. Dignac, Is soil carbon mostly root carbon? Mechanisms for a specific stabilisation. *Plant Soil* **269**, 341–356 (2005).

8. N. W. Sokol, Sara. E. Kuebbing, E. Karlsen-Ayala, M. A. Bradford, Evidence for the primacy of living root inputs, not root or shoot litter, in forming soil organic carbon. *New Phytol* **221**, 233–246 (2019).

9. M. W. I. Schmidt, J. O. Skjemstad, C. Jäger, Carbon isotope geochemistry and nanomorphology of soil black carbon: Black chernozemic soils in central Europe originate from ancient biomass burning. *Global Biogeochemical Cycles* **16** (2002).

10. S. Dreibrodt, R. Hofmann, M. Dal Corso, H.-R. Bork, R. Duttmann, S. Martini, P. Saggau, L. Schwark, L. Shatilo, M. Videiko, M.-J. Nadeau, P. M. Grootes, W. Kirleis, J. Müller, Earthworms, Darwin and prehistoric agriculture-Chernozem genesis reconsidered. *Geoderma* **409**, 115607 (2022).

11. J. P. Lynch, T. Wojciechowski, Opportunities and challenges in the subsoil: pathways to deeper rooted crops. *Journal of Experimental Botany* **66**, 2199–2210 (2015).

12. C. D. Sprunger, L. G. Oates, R. D. Jackson, G. P. Robertson, Plant community composition influences fine root production and biomass allocation in perennial bioenergy cropping systems of the upper Midwest, USA. *Biomass and Bioenergy* **105**, 248–258 (2017).

13. P. Smith, Soil carbon sequestration and biochar as negative emission technologies. *Glob Change Biol* **22**, 1315–1324 (2016).

14. I. A. Shabtai, R. C. Wilhelm, S. A. Schweizer, C. Höschen, D. H. Buckley, J. Lehmann, Calcium promotes persistent soil organic matter by altering microbial transformation of plant litter. *Nat Commun* **14**, 6609 (2023).

15. M. C. Rowley, S. Grand, É. P. Verrecchia, Calcium-mediated stabilisation of soil organic carbon. *Biogeochemistry* **137**, 27–49 (2018).

16. M. C. Rowley, S. Grand, J. E. Spangenberg, E. P. Verrecchia, Evidence linking calcium to increased organo-mineral association in soils. *Biogeochemistry* **153**, 223–241 (2021).

17. C. Rasmussen, K. Heckman, W. R. Wieder, M. Keiluweit, C. R. Lawrence, A. A. Berhe, J. C. Blankinship, S. E. Crow, J. L. Druhan, C. E. Hicks Pries, E. Marin-Spiotta, A. F. Plante, C. Schädel, J. P. Schimel, C. A.

Sierra, A. Thompson, R. Wagai, Beyond clay: towards an improved set of variables for predicting soil organic matter content. *Biogeochemistry* **137**, 297–306 (2018).

18. S. F. von Fromm, A. M. Hoyt, G. E. Acquah, E. Aynekulu, A. A. Berhe, S. M. Haefele, M. Lange, S. P. McGrath, K. D. Shepherd, A. M. Sila, J. Six, E. K. Towett, S. E. Trumbore, T.-G. Vågen, E. Weullow, L. A. Winowiecki, S. Doetterl, "Continental-scale controls on soil organic carbon across sub-Saharan Africa" (preprint, Soils and biogeochemical cycling, 2020); https://doi.org/10.5194/soil-2020-69.

19. J. G. Bockheim, "Mollic Epipedon" in *Soil Geography of the USA* (Springer International Publishing, Cham, 2014; https://link.springer.com/10.1007/978-3-319-06668-4_5), pp. 29–46.

20. D. B. Smith, W. F. Cannon, Geochemical and Mineralogical Data for Soils of the Conterminous United States.

21. Soil Survey Staff, Gridded National Soil Survey Geographic (gNATSGO) Database for the Conterminous United States.

22. S. Wills, T. Loecke, C. Sequeira, G. Teachman, S. Grunwald, L. T. West, "Overview of the U.S. Rapid Carbon Assessment Project: Sampling Design, Initial Summary and Uncertainty Estimates" in *Soil Carbon*, A. E. Hartemink, K. McSweeney, Eds. (Springer International Publishing, Cham, 2014; http://link.springer.com/10.1007/978-3-319-04084-4_10), pp. 95–104.

23. National Cooperative Soil Survey, National Cooperative Soil Survey Soil Characterization Database (2018). http://ncsslabdatamart.sc.egov.usda.gov/.

24. J.-F. Lamarque, F. Dentener, J. McConnell, C.-U. Ro, M. Shaw, R. Vet, D. Bergmann, P. Cameron-Smith, S. Dalsoren, R. Doherty, G. Faluvegi, S. J. Ghan, B. Josse, Y. H. Lee, I. A. MacKenzie, D. Plummer, D. T. Shindell, R. B. Skeie, D. S. Stevenson, S. Strode, G. Zeng, M. Curran, D. Dahl-Jensen, S. Das, D. Fritzsche, M. Nolan, Multi-model mean nitrogen and sulfur deposition from the Atmospheric Chemistry and Climate Model Intercomparison Project (ACCMIP): evaluation of historical and projected future changes. *Atmos. Chem. Phys.* **13**, 7997–8018 (2013).

25. N. RAMANKUTTY, J. A. FOLEY, ISLSCP II Potential Natural Vegetation Cover. ORNL Distributed Active Archive Center [Preprint] (2010). https://doi.org/10.3334/ORNLDAAC/961.

26. E. W. Slessarev, O. A. Chadwick, N. W. Sokol, E. E. Nuccio, J. Pett-Ridge, Rock weathering controls the potential for soil carbon storage at a continental scale. *Biogeochemistry* **157**, 1–13 (2022).

27. Z. Ratajczak, J. B. Nippert, J. M. Briggs, J. M. Blair, Fire dynamics distinguish grasslands, shrublands and woodlands as alternative attractors in the C entral G reat P lains of N orth A merica. *Journal of Ecology* **102**, 1374–1385 (2014).

28. A. C. Staver, S. Archibald, S. Levin, Tree cover in sub-Saharan Africa: Rainfall and fire constrain forest and savanna as alternative stable states. *Ecology* **92**, 1063–1072 (2011).

29. FAO/UNESCO, FAO Soil map of the world (1974).

30. E. W. Slessarev, Y. Lin, N. L. Bingham, J. E. Johnson, Y. Dai, J. P. Schimel, O. A. Chadwick, Water balance creates a threshold in soil pH at the global scale. *Nature* **540**, 567–569 (2016).

31. E. W. Slessarev, X. Feng, N. L. Bingham, O. A. Chadwick, Landscape Age as a Major Control on the Geography of Soil Weathering. *Global Biogeochem. Cycles* **33**, 1513–1531 (2019).

32. J. G. Bockheim, *Soils of the Laurentian Great Lakes, USA and Canada* (Springer International Publishing, Cham, 2021; http://link.springer.com/10.1007/978-3-030-52425-8).

33. P. M. Jacobs, J. A. Mason, Impact of Holocene dust aggradation on A horizon characteristics and carbon storage in loess-derived Mollisols of the Great Plains, USA. *Geoderma* **125**, 95–106 (2005).

34. M. J. Cooke, L. A. Stern, J. L. Banner, L. E. Mack, Evidence for the silicate source of relict soils on the Edwards Plateau, central Texas. *Quat. res.* **67**, 275–285 (2007).

35. R. C. Capo, O. A. Chadwick, Sources of strontium and calcium in desert soil and calcrete. *Earth and Planetary Science Letters* **170**, 61–72 (1999).

36. J. C. Neff, A. P. Ballantyne, G. L. Farmer, N. M. Mahowald, J. L. Conroy, C. C. Landry, J. T. Overpeck, T. H. Painter, C. R. Lawrence, R. L. Reynolds, Increasing eolian dust deposition in the western United States linked to human activity. *Nature Geosci* **1**, 189–195 (2008).

37. S. Albani, N. M. Mahowald, L. N. Murphy, R. Raiswell, J. K. Moore, R. F. Anderson, D. McGee, L. I. Bradtmiller, B. Delmonte, P. P. Hesse, P. A. Mayewski, Paleodust variability since the Last Glacial Maximum and implications for iron inputs to the ocean. *Geophysical Research Letters* **43**, 3944–3954 (2016).

38. D. R. Muhs, E. A. Bettis, Geochemical Variations in Peoria Loess of Western Iowa Indicate Paleowinds of Midcontinental North America during Last Glaciation. *Quat. res.* **53**, 49–61 (2000).

39. M. Haines, P. Fishback, P. Rhode, United States Agriculture Data, 1840 - 2012: Version 4, version v4, ICPSR - Interuniversity Consortium for Political and Social Research (2014); https://doi.org/10.3886/ICPSR35206.V4.

40. T. O. West, A. C. McBride, The contribution of agricultural lime to carbon dioxide emissions in the United States: dissolution, transport, and net emissions. *Agriculture, Ecosystems & Environment* **108**, 145–154 (2005).

41. J. H. Kim, E. G. Jobbágy, D. D. Richter, S. E. Trumbore, R. B. Jackson, Agricultural acceleration of soil carbonate weathering. *Glob. Change Biol.* **26**, 5988–6002 (2020).

42. S. Raza, N. Miao, P. Wang, X. Ju, Z. Chen, J. Zhou, Y. Kuzyakov, Dramatic loss of inorganic carbon by nitrogen-induced soil acidification in Chinese croplands. *Global Change Biology* **26**, 3738–3751 (2020).

43. K. Zamanian, M. Zarebanadkouki, Y. Kuzyakov, Nitrogen fertilization raises CO_2 efflux from inorganic carbon: A global assessment. *Global Change Biology* **24**, 2810–2817 (2018).

44. L. L. Taylor, J. Quirk, R. M. S. Thorley, P. A. Kharecha, J. Hansen, A. Ridgwell, M. R. Lomas, S. A. Banwart, D. J. Beerling, Enhanced weathering strategies for stabilizing climate and averting ocean acidification. *Nature Clim Change* **6**, 402–406 (2016).

45. Z. Liu, G. L. Macpherson, C. Groves, J. B. Martin, D. Yuan, S. Zeng, Large and active CO2 uptake by coupled carbonate weathering. *Earth-Science Reviews* **182**, 42–49 (2018).

46. R. Paradelo, I. Virto, C. Chenu, Net effect of liming on soil organic carbon stocks: A review. *Agriculture, Ecosystems & Environment* **202**, 98–107 (2015).

47. N. W. Sokol, J. Sohng, K. Moreland, E. Slessarev, H. Goertzen, R. Schmidt, S. Samaddar, I. Holzer, M. Almaraz, E. Geoghegan, B. Houlton, I. Montañez, J. Pett-Ridge, K. Scow, Reduced accrual of mineral-associated organic matter after two years of enhanced rock weathering in cropland soils, though no net losses of soil organic carbon. *Biogeochemistry* **167**, 989–1005 (2024).

48. S. S.-E. Tsao, T. J. Surhoff, G. Amatulli, M. Almaraz, J. Gewirtzman, B. Woollen, E. W. Slessarev, J. E. Saiers, C. T. Reinhard, S. Zhang, N. J. Planavsky, P. A. Raymond, A spatially explicit dataset of agriculture liming across the contiguous United States. ESSD – Land/Land cover and land use [Preprint] (2025). https://doi.org/10.5194/essd-2025-411.

49. B. Labaz, A. E. Hartemink, Y. Zhang, A. Stevenson, C. Kabała, Organic carbon in Mollisols of the world − A review. *Geoderma* **447**, 116937 (2024).

50. Q. Yu, L. You, U. Wood-Sichra, Y. Ru, A. K. B. Joglekar, S. Fritz, W. Xiong, M. Lu, W. Wu, P. Yang, A cultivated planet in 2010 – Part 2: The global gridded agricultural-production maps. *Earth Syst. Sci. Data* **12**, 3545–3572 (2020).

51. FAO, Annex I: Food Composition Tables. https://www.fao.org/4/x9892e/X9892e05.htm.

52. L. T. C. Bonten, G. J. Reinds, M. Posch, A model to calculate effects of atmospheric deposition on soil acidification, eutrophication and carbon sequestration. *Environmental Modelling & Software* **79**, 75–84 (2016).

53. M. B. Bertagni, S. Calabrese, G. Cipolla, L. V. Noto, A. Porporato, Advancing Enhanced Weathering Modeling in Soils: Critical Comparison With Experimental Data. *J Adv Model Earth Syst* **17**, e2024MS004224 (2025).

54. Prism Climate Group, Oregon State University, Prism climate data (2011).

55. H. E. Beck, A. De Roo, A. I. J. M. Van Dijk, Global Maps of Streamflow Characteristics Based on Observations from Several Thousand Catchments*. *Journal of Hydrometeorology* **16**, 1478–1501 (2015).

56. B. Martens, D. G. Miralles, H. Lievens, R. Van Der Schalie, R. A. M. De Jeu, D. Fernández-Prieto, H. E. Beck, W. A. Dorigo, N. E. C. Verhoest, GLEAM v3: satellite-based land evaporation and root-zone soil moisture. *Geosci. Model Dev.* **10**, 1903–1925 (2017).

57. M. Zhao, S. Running, F. A. Heinsch, R. Nemani, "MODIS-Derived Terrestrial Primary Production" in *Land Remote Sensing and Global Environmental Change*, B. Ramachandran, C. O. Justice, M. J. Abrams, Eds. (Springer New York, New York, NY, 2010; http://link.springer.com/10.1007/978-1-4419-6749-7_28)vol. 11 of *Remote Sensing and Digital Image Processing*, pp. 635–660.

58. D. P. Swaney, R. W. Howarth, B. Hong, Nitrogen use efficiency and crop production: Patterns of regional variation in the United States, 1987–2012. *Science of The Total Environment* **635** (2018).

59. D. B. Schwede, G. G. Lear, A novel hybrid approach for estimating total deposition in the United States. *Atmospheric Environment* **92**, 207–220 (2014).

60. H. Haario, M. Laine, A. Mira, E. Saksman, DRAM: Efficient adaptive MCMC. *Stat Comput* **16**, 339–354 (2006).

61. K. Soetaert, T. Petzoldt, Inverse Modelling, Sensitivity and Monte Carlo Analysis in *R* Using Package **FME**. *J. Stat. Soft.* **33** (2010).

62. A. Gelman, Scaling regression inputs by dividing by two standard deviations. *Statistics in Medicine* **27**, 2865–2873 (2008).

63. T. J. DiCiccio, B. Efron, Bootstrap confidence intervals. *Statist. Sci.* **11** (1996).

64. N. C. Brady, R. R. Weil, *The Nature and Properties of Soils* (Pearson, Harlow, England London New York, Fifteenth edition, global edition., 2016)*Pearson global edition*.

Acknowledgments

Funding:

LLNL Laboratory Directed Research and Development grant 22-ERD-19 (EWS, KG)

LLNL Laboratory Directed Research and Development program 24-SI-002 (JP)

DOE Carbon Negative Energy Earthshot Research Center SCW1841 (JP)

Work at LLNL was performed under the auspices of the DOE, Contract DE-AC52-07NA27344.

Author contributions:

Conceptualization: EWS, HRG, RL, KJM, JP, NS, DZ, KG
Methodology: EWS, KG
Investigation: EWS
Visualization: EWS
Supervision: EWS, KG
Writing—original draft: EWS
Writing—review & editing: EWS, HRG, RL, KJM, JP, NS, DZ, KG

Competing interests: Authors declare that they have no competing interests.

Data and materials availability: The R code used to perform these analyses is available at https://github.com/eslessarev/Calcium-promotes-carbon-rich-grassland-soil-R-Code.

Figures and Tables

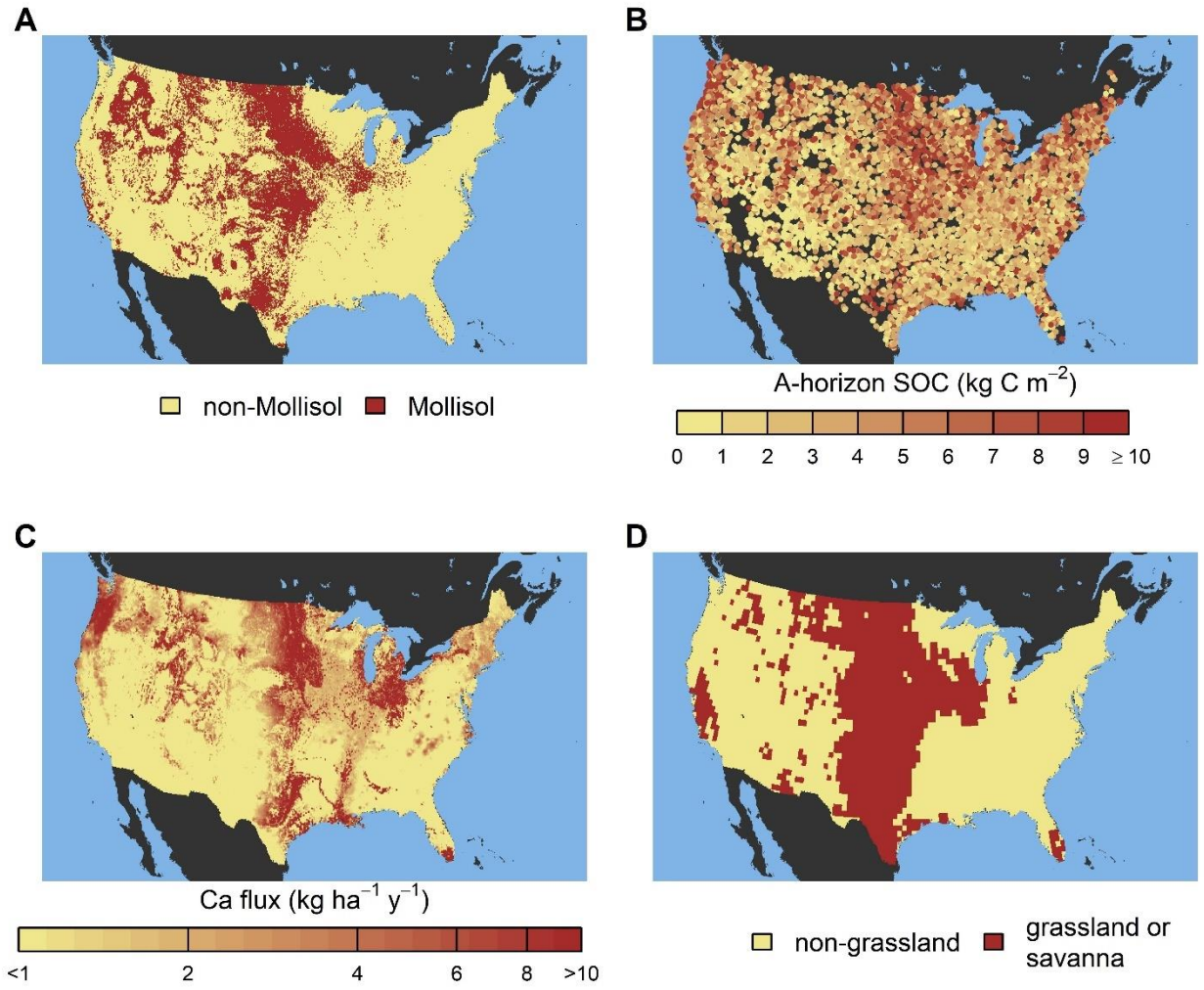

Fig. 1. Potential environmental controls on Mollisols across the USA. (A) The distribution of the Mollisol soil order across the conterminous USA based on digital soil mapping (*21*). **(B)** Point observations of A-horizon soil organic carbon (SOC) derived from two databases (*22*, *23*). **(C)** Modeled preindustrial available calcium flux from silicate weathering, carbonate weathering, and atmospheric deposition. **(D)** The potential distribution of grasslands and savannas (*25*).

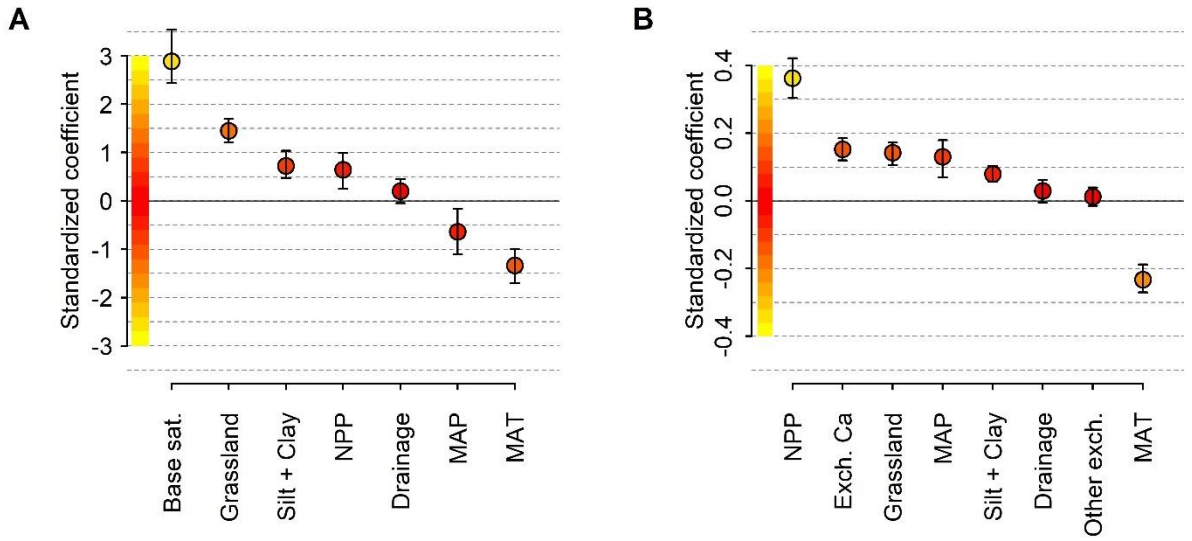

Fig. 2. Controls on Mollisol distribution and A-horizon soil organic carbon stocks in the USA. (A) Standardized regression coefficients derived from a multivariate logistic regression model, where the presence or absence of Mollisols was predicted as a function of the seven variables listed on the horizonal axis. **(B)** Standardized regression coefficients derived from a multivariate linear regression model, where A-horizon organic carbon stocks were predicted as a function of the eight variables listed on the horizonal axis. In both panels, whiskers show 95% confidence intervals derived from a spatial blocked bootstrapping procedure (see Materials and Methods). Standardization was performed by dividing each non-binary variable by two times the standard deviation.[49] The absolute value of each regression coefficient is an index of how strongly related each variable is to the response variable, and is shown with a relative color scale: yellow = maximum, red = zero. Abbreviations: Base sat. = base saturation, NPP = net primary productivity, MAT = mean annual temperature, MAP = mean annual precipitation, Exch. Ca = total exchangeable Ca, Other exch. = sum of non-Ca exchangeable ions.

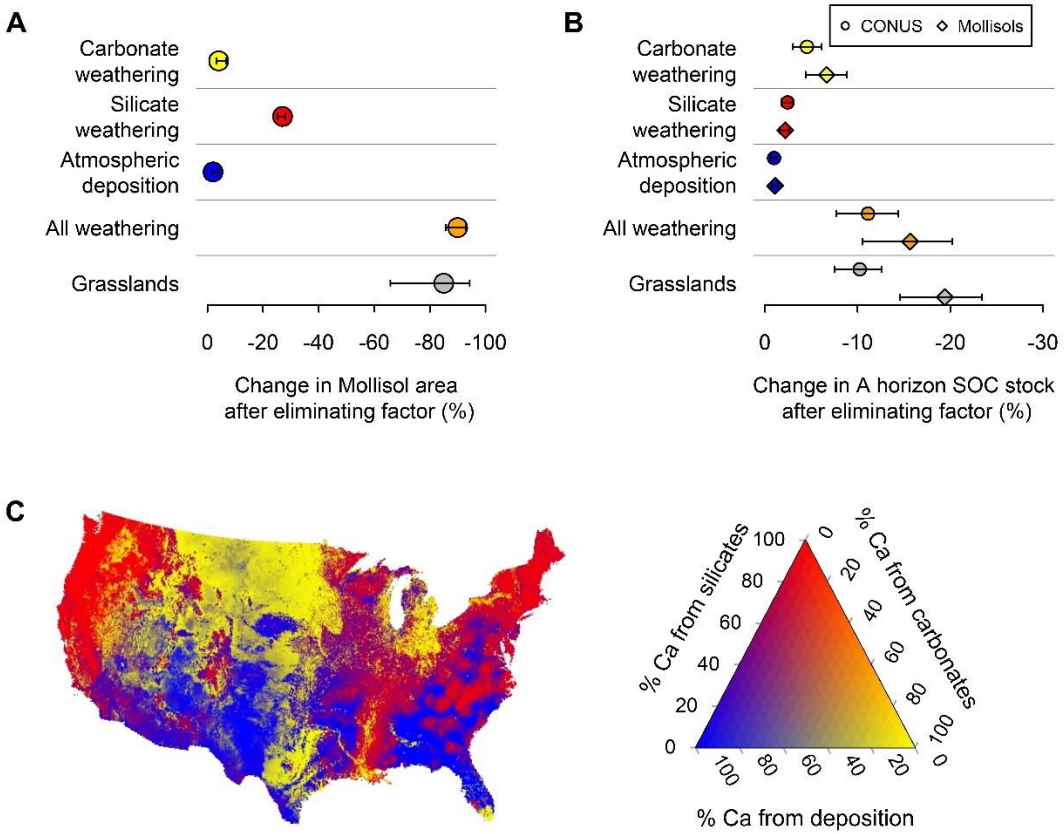

Fig. 3. Sources of available Ca and their effect on Mollisol extent across the USA. **(A)** The relative effect of removing Ca sources on predicted Mollisol area and the effect of eliminating grasslands. **(B)** The relative effect of removing the same set of environmental factors on total A-horizon soil organic carbon across the conterminous USA (CONUS; circles) and Mollisol areas only (diamonds). Whiskers show 95% confidence intervals derived from spatial blocked bootstrapping (see Methods). (C) The relative contributions of carbonate weathering, silicate weathering, and atmospheric deposition to available Ca across the USA. Across all panels red = silicate weathering, yellow = carbonate weathering, and blue = deposition.

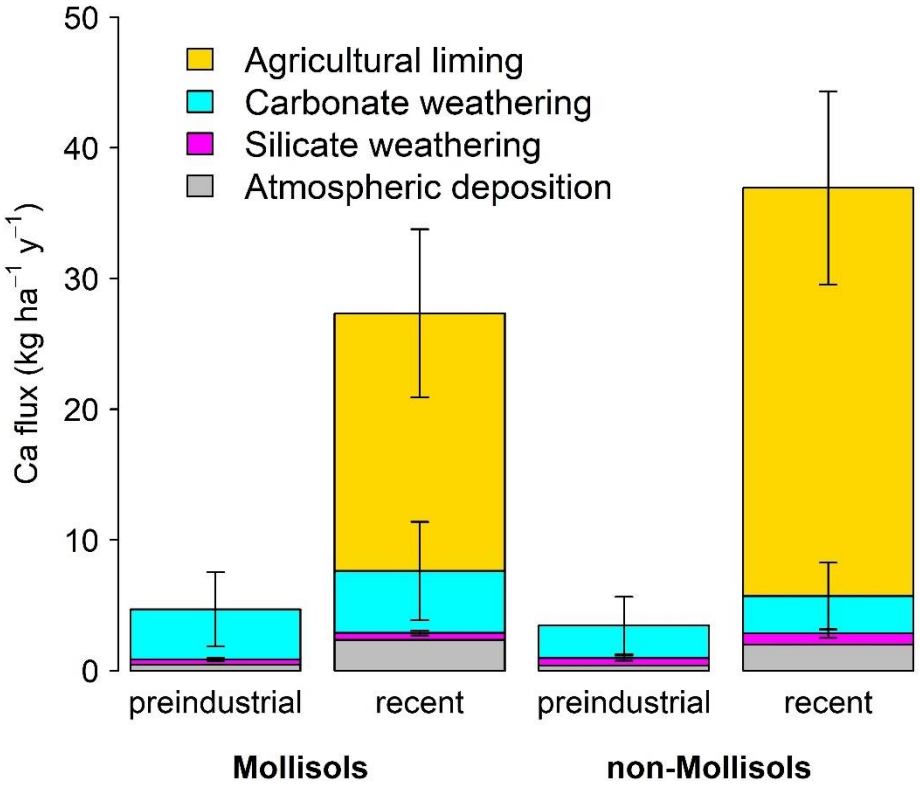

Fig. 4. Modeled available Ca fluxes to croplands, preindustrial (1850) versus recent (2000-2010). Stacked bars show the Ca sources: atmospheric deposition, carbonate weathering, silicate weathering, and agricultural liming. Data for Mollisol regions are shown on the left and non-Mollisol regions on the right. Whiskers show standard error estimates for each quantity derived from a Monte Carlo uncertainty analysis assuming +/- 20% variability in the model inputs and parameters. Liming estimates are based on the conservative assumption that farmers lime sufficiently to maintain soil pH (see Supplementary Materials).

Supplementary Materials for

Calcium promotes carbon-rich grassland soils

Eric W. Slessarev *et al.*

*Corresponding author. Email: eric.slessarev@yale.edu

This supplement includes:

Supplementary Text
Figs. S1 to S5
Tables S1 to S7
References (1 to 34)

Supplementary Text: Geochemical model description

Governing equations

Our model was specified to track inputs and outputs of seven ions that control soil pH and weathering rates: Ca^{2+}, Mg^{2+}, Na^{+}, K^{+}, SO_4^{2-}, NO_3^{-}, Cl^{-} (Table S3). These ions were sourced from dissolution of silicate and carbonate minerals, atmospheric deposition, agricultural inputs, and biological fixation in the case of N. Ions were lost via leaching, carbonate mineral precipitation, export in crop biomass, and volatilization in the case of N. Additional ions were assumed to equilibrate instantaneously with the soil solution and hence were modeled implicitly as a function of other factors: H^{+}, Al^{3+}, $Al(OH)^{2+}$, $Al(OH)_2^{+}$, AlH_2Org^{2+}, $AlHOrg^{+}$, OH^{-}, CO_3^{-}, HCO_3^{-}, H_2Org^{-}, $HOrg^{2-}$, Org^{3-}, $Al(OH)_4^{-}$.

Hydrology

We parametrized leaching rates for major ions as a function of recharge or hydrologic baseflow (RC, mm y^{-1}), which we assume represents the flux of water that infiltrates the soil without being lost to evapotranspiration or overland flow. We partitioned the total amount of soil water (V, l) into mobile and immobile components, under the assumption that only a fraction of the soil pores are leached during leaching events. The immobile component of the soil water was equal to the water content at wilting point (V_{wp}, l), which governed the fraction of soil water mobilized during recharge:

$$F_{mob} = (V - V_{wp})/V \qquad \text{(Equation 1)}$$

We assumed that only the solutes in the mobile fraction are vulnerable to leaching loss and that solutes are partitioned into mobile and immobile fractions by F_{mob}. We also assumed that solutes in the mobile fraction are conservatively diluted at the timescale of recharge events. The concentration of solute i leached during recharge events (C_i) was therefore a function of the soil moisture at field capacity, V_{fc}:

$$C_i = M_i * F_{mob}/(V_{fc} - V_{wp}) \qquad \text{(Equation 2)}$$

Where M_i was the total moles of the solute in the soil. The leaching rate for a given ion, L_i (mol y^{-1}) was a function of concentration in recharge water (mol l^{-1}) times recharge (l y^{-1}):

$$L_i = RC * C_i \qquad \text{(Equation 3)}$$

Weathering kinetics

Weathering kinetic expressions vary widely in complexity. We adopted a simple power law description for silicate weathering kinetics. More complex approaches, such as transition state theory, incorporate multiple reaction mechanisms. These approaches are sensitive to assumptions regarding the type and reactivity of secondary minerals and the extent of mineral surface passivation, which we could not parametrize at the scale of the USA. To further reduce complexity, dissolution kinetics of tectosilicates and inosilicates were referenced to the reactivity of plagioclase feldspar based on a compilation of field-based weathering rate measurements (*1*). This was not possible for pyroxene given a lack of field based weathering rate estimates, so we assigned this mineral a reaction rate of 1.0 relative to plagioclase. For tecto- or inosilicate mineral i, weathering rates in the top 100 cm of soil (mol y^{-1}) were a function of total geometric surface area (A_i, m^2), a reaction rate coefficient (r_1, mol m^{-2} y^{-1}), the ratio giving reaction rate relative to plagioclase (RR_i, unitless), an Arrhenius-type term governing temperature dependence (T_f, unitless), volumetric water content (θ m^3 m^{-3}), the hydrogen ion concentration ($[H^+]$), a reference hydrogen ion concentration ($[H^+_r]$, set equal to 10^{-5}), and the reaction order with respect to H^+ (n).

$$W_i = A_i * r_1 * RR_i * T_f * \theta * (H^+/H^+_r)^n \quad \text{(Equation 4)}$$

For phyllosilicate minerals, the rate expression was identical except that the term RR_i was omitted and an affinity term was added to make the reactions reversible, allowing clay synthesis.

$$W_{i,\,phyllo} = A_i * r_2 * T_f * \theta * (H^+/H^+_r)^n * (1 - \Omega_i) \quad \text{(Equation 5)}$$

The term r_2 gives a reaction rate coefficient for phyllosilicates. The parameter Ω_i was the saturation index for phyllosilicate mineral i, where $\Omega_i = IAP_i/K_{sp}$. The IAP was the ion activity product or reaction quotient. K_{sp} was the solubility constant for each mineral.

We assumed that the temperature and pH dependence of silicate weathering was the same for all minerals. The activation energy for silicate weathering was set to equal 74 kJ mol^{-1} K^{-1} (*2*). The temperature modifier for silicate weathering was given by the following equation:

$$T_f = \exp(-Ea_{sil}/R * (1/(T) - 1/(T_{ref}))) \quad \text{(Equation 6)}$$

Where Ea_{sil} was the activation energy for silicates, R was the universal gas constant, T was the soil temperature approximated as the mean annual air temperature (K) and T_{ref} was a reference temperature (298 K).

We assigned several silicate weathering parameters manually in order to match published compilations of field weathering rates (*3*, *4*). The parameter r_1 represented the bulk plagioclase feldspar weathering rate coefficient (y^{-1}) at a reference pH of 5.0 ($H_{ref} = 10^{-5}$). We assumed that under the wettest climate conditions, mean soil pH approaches a value of 5.0 (*5*), and so bulk feldspar weathering rates ought to approach r_1 under these conditions. Across our calibration dataset, the 95th percentile value for recharge (RC) equaled 474 mm, which implies that r_1 equals $10^{-4.3}$ based on the power law relationship between recharge and bulk weathering rates reported by Yu and Hunt (2018) (*4*). Based on similar reasoning, we set the reaction order for H^+, n, equal to 0.66. We chose this value because field estimates of silicate weathering rates increase by roughly two orders of magnitude in the transition from dry conditions (infiltration rates ~ 0.1 m y^{-1}) to humid conditions (infiltration rates ~ 1 m y^{-1}) (*3*), and soil pH spans roughly 3 units in the transition from wet to dry climates (*5*), This implies that weathering rates should increase by two orders of magnitude over a three order of magnitude range in pH (reaction order = 0.66). This value is reasonable for many silicates (*6*), and allowed us to recover the observed relationship between feldspar weathering rates in the field and infiltration reasonably well with the calibrated model (Figure S4).

We modeled carbonate weathering kinetics using a more complex expression based on transition state theory because carbonate minerals dissolve and precipitate congruently in soil, reducing uncertainty regarding secondary minerals and surface passivation. Dissolution and precipitation for carbonate minerals was governed by the following equation:

$$W_{i,\,carb} = A_i * r_3 * \theta * (R_{acid} * [H^+]^{nH} + R_{neutral} + R_{CO2} * pCO_2^{nCO2}) * (1 - \Omega_i) \quad \text{(Equation 7)}$$

Where A_i was the total surface area for mineral i, r_3 was ratio of reactive surface area to geometric surface area for carbonates, R_{acid}, $R_{neutral}$, and R_{CO2} were separate reaction mechanisms for acid, neutral, and CO_2 driven dissolution reactions, nH was the reaction order for H^+, and nCO_2 was the reaction order for CO_2. The parameter Ω_i was the saturation index for carbonate mineral i, where

$\Omega_i = IAP_i/K_{sp}$. The IAP was the ion activity product or reaction quotient. K_{sp} was the solubility constant for each mineral. Reaction mechanisms (R_m) were governed by equations with the form:

$$R_m = A_m*\exp(-Ea_m/R*(1/(T) - 1/(T_{ref}))) \quad \text{(Equation 8)}$$

Where A_m and Ea_m were the preexponential factor (mol m^{-2} y) and activation energy (kJ mol^{-1} K^{-1}) for mechanism m.

All spatially invariant parameters related to weathering reactions are given in Table S5. Our treatment of weathering kinetics left two unknown parameters: r_2, the reaction rate coefficient for phyllosilicates, and r_3, the ratio of reactive to total surface area for carbonates. These parameters were obtained by model inversion (see Methods in main article).

Mineral surface areas

We estimated geometric surface areas for each mineral. For tectosilicates, inosilicates, and carbonates, we assumed that particles were silt- and sand-sized and spherical. We calculated surface area to volume ratios (SVR, m^2 m^{-3}) for silt and sand:

$$SVR = (4* \pi *(D/2)^2)/(4/3*\pi* (D/2)^3) \quad \text{(Equation 9)}$$

Where D was the particle diameter, which we set to the geometric mean of each size class (*7*). The average surface area to volume ratio for minerals in the silt and sand fraction was then calculated as a weighted average based on silt and sand percentages derived from the NATSGO database (see below). Clays (illite and chlorite) were modeled as cylindrical plates with a diameter of 1 um and a diameter to height ratio of 10:1 (*7*):

$$SVR_{clay} = ((D/10*2*\pi*D/2) + (2*\pi*(D/2)^2))/((D/10)*(\pi*(D/2)^2)) \quad \text{(Equation 10)}$$

Total geometric surface area for each mineral was obtained by multiplying the surface area to volume ratio by the total volume of each mineral in the soil.

$$A_i = SVR_i*P_i*(\rho_s/\rho_i)*h*10^{-5} \quad \text{(Equation 11)}$$

Where P_i was the percentage of mineral i in the soil, ρ_s was the bulk density of the soil, ρ_i was the density of mineral i, and h was the soil thickness in mm. Chemical formulas and densities for the minerals that we included in the model are shown in Table S6. For clay minerals, we limited our analysis to chlorite (clinochlore) and illite (approximated as muscovite), which we treated as generalized categories that stand in for the full diversity of Mg- and K-bearing 2:1 phyllosilicates (e.g. vermiculite and smectite group clays).

Equilibrium chemistry

We parametrized a set of major equilibrium reactions that governed carbonate ion speciation, aluminum hydrolysis, organic acid speciation, Al-organo ion pair formation, and cation exchange reactions (Table S7). When possible, we obtained equilibrium constants by calculating them from standard enthalpies and entropies, which we obtained from the SUPCRT92 thermodynamic database (*8*) loaded with the R package CHNOSZ (*9*).

Carbonate equilibria depended on the average soil pCO_2, which we parametrized as a function of soil respiration (*10*):

$$pCO_2 = pCO_{2atm} + 1.03*Rs/T^2 \quad \text{(Equation 12)}$$

Where pCO_{2atm} was atmospheric pCO_2, set to 380 ppm for 2001-2010 (*11*) and 280 ppm for preindustrial times (*12*), and R_s was soil respiration in g m^{-2} y^{-1}. We obtained R_s from net primary productivity (NPP, g m^{-2} y^{-1}) (*13*):

$$R_s = 1.24*NPP + 24.5 \quad \text{(Equation 13)}$$

We modeled dissolution and precipitation of carbonates and phyllosilicates as reversible processes governed by chemical equilibria (Table S7), which defined the saturation index (Ω) used in weathering rate calculations. In the case of phyllosilicates, the saturation state depended on dissolved H_4SiO_2, which we did not model explicitly as a state variable. Instead, the concentration of H_4SiO_2 was assumed to be determined by instantaneous dissolution and precipitation of secondary amorphous SiO_2 (Table S7).

We represented organic acid speciation using the triprotic model and allowed for formation of ion pairs between Al^{3+} and organic acids. Equilibrium constants for these reactions were obtained by averaging published values from New England lakes, streams, and soils (*14*). To parametrize equilibrium reactions involving organic acids, we estimated the amount of dissolved organic carbon and then calculated total organic acid charge (Org_{tot}, moles charge) from total DOC (moles). We converted DOC to Org_{tot} based on a charge density (m = 0.049 mol mol^{-1}) averaged from the New England water survey (*14*). We approximated soil DOC concentrations by assuming that DOC inputs are equal to NPP, reasoning that over the long run all plant inputs to soil must be converted to DOC before they are respired or sequestered. We then assumed that DOC decays as a first order process and is lost due to leaching:

$$dDOC/dt = NPP - k_{DOC}*Q_{10}^{((T-293)/10)}*DOC - DOC*RC*F_{mob}/(V_{fc} - V_{wp}) \quad \text{(Equation 14)}$$

Where k_{DOC} was a decay constant and Q_{10} defined the temperature dependence of DOC decay. We obtained k_{DOC} by taking the geometric mean of previously reported "fast" and "slow" DOC decay constants (*15*). Assuming that DOC is maintained at steady state for our purposes, the organic acid concentration (molc l^{-1}) was obtained from the following equation:

$$Org_{tot} = m*(NPP/12.01)/(1 + k_{DOC}*Q_{10}^{((T-293)/10)})*(1/V) \quad \text{(Equation 15)}$$

Exchange reactions were specified using the Gaines-Thomas approach. We parameterized cation exchange reactions using an existing compilation (*16*), which summarized Gaines-Thomas exchange constants for sand, loess (silt enriched), and clay dominated soils in the Netherlands. As a first order approximation, we assigned exchange constants by calculating the weighted mean of the profile-averaged constants listed in the compilation, with weights given by the sand, silt, and clay fractions obtained from NATSGO.

When calibrating the model, we simulated re-equilibration of soil pH with laboratory conditions because in-situ pH and laboratory-measured pH can vary substantially (*17*). To do this, we fixed soil water content so that the soil mass to water ratio equaled 1:1, set the temperature to 20°C, and adjusted pCO_2 to reflect the ambient atmospheric concentration. Concentrations of conserved ions were adjusted to reflect the change in soil water content during measurement. Charge balance and exchange reactions were solved based on laboratory parameters to yield laboratory pH. In cases where the soil contained calcite, we assumed that calcite could partially buffer pH at the timescale of laboratory measurement. This assumption is supported by a global pH compilation, which shows that pH approximates a calcite-buffered value when carbonates are present in even small

amounts (*5*). To represent carbonate buffering in the lab, we fixed the saturation index for calcite so that it would equal its value in the field and then solved for the equilibrium Ca concentration at the laboratory pCO_2 and temperature.

Nutrient budgets

While our main goal was to model pre-agricultural Ca weathering across the USA, we considered nutrient inputs and outputs in modern croplands to assist with model calibration and to help us understand how Ca fluxes have changed over time. Nitrogen had the most complex nutrient budget. To simplify N accounting, we assumed that all reduced N is completely nitrified following DON export; hence all N is treated as NO_3^- (*18*). In natural systems, the only N inputs in the model were atmospheric deposition and nitrogen fixation (F_N, mol m^{-2} y^{-1}), which we modeled as a function of NPP (*19*):

$$F_N = 1.8*(1 - \exp(-0.003*NPP))/14.01 \quad \text{(Equation 16)}$$

In addition to leaching of NO_3^-, we considered leaching of organic N, which we assume happens before nitrification. We assigned a molar CN ratio of 20, which is typical for dissolved organic matter (*20*), and modeled DON export as a function of DOC leaching:

$$L_N = N*RC*F_{mob}/(V_{fc} - V_{wp}) + DOC/CN_{DOM}*RC*F_{mob}/(V_{fc} - V_{wp}) \quad \text{(Equation 17)}$$

Because we fixed the CN ratio for DOM, DON export could exceed inputs, leading to negative NO_3^- concentrations. In these cases, we forced DON export to equal inputs and NO_3^- concentrations equaled zero.

In croplands, we considered N inputs from fertilizer, manure, crop N fixation, free living N fixation, and N removal in crop biomass:

$$C_N = N_{fert} + N_{man} + N_{fix,crop} + N_{fix,free} - N_{rem} \quad \text{(Equation 18)}$$

The first three of these parameters as well as the N removal rate varied spatially and were taken from a published county-level compilation (*21*) whereas free-living N fixation rates were approximated at 0.036 mol m^{-2} y^{-1} (*22*) and did not vary spatially. The parameter N_{man} was set equal to 20% of total manure N to account for inefficiency in manure recovery (*23*).

Nitrogen can be lost from soil via ammonia volatilization, NO_x emission, and denitrification to N_2O or N_2. The processes governing these fluxes are complex and representing them in detail was beyond the scope of our effort. Instead, we manually calibrated a single parameter, r_v, that controlled the N volatilization rate:

$$V_N = N/N_{inputs}*r_v \quad \text{(Equation 19)}$$

The expression was based on the assumption that N volatilization is proportional to the total available N pool but inversely proportional to N inputs. We reasoned that as N inputs increase, the opportunity for denitrification and ammonia volatilization would be lower because more N would escape the soil before volatilization. This is consistent with the observation that low-input ecosystems volatilize a greater fraction of N than high-input agricultural systems (*24*). We selected a value of 0.3 y^{-1} for r_v, which ensured plausible nitrate stocks for the top 1 meter of soil: in the range of 100-200 kg NO_3^--N ha^{-1} in croplands (*25*, *26*) and less than 10 kg NO_3^--N ha^{-1} in forests (*27*).

Nitrogen removal in harvest could sometimes exceed N inputs, leading to implausibly low NO_3^- concentrations. At locations where N surplus in croplands was less than 0.1 mol m^{-2} y^{-1}, we assumed that imbalances in the N budget were being met by an unknown source (e.g., decomposition of soil organic matter or higher than 20% manure recoverability). In these cases, we assigned a minimum value of 0.1 mol m^{-2} y^{-1} for the net nitrogen balance before applying losses from NO_3^- leaching and volatilization. This minimum value maintained cropland NO_3^- levels within reported ranges (*25*, *26*).

Cropland C budgets were also adjusted to account for import and export of C in agriculture. We adjusted NPP in croplands to account for removal of crop biomass, which accounts for 43% of cropland NPP (*28*). We also accounted for C introduced with manure. We assumed a molar C:N ratio of 10 for manure, and used this number to scale manure C based on county-level estimates for manure N.

We also considered cropland nutrient budgets for some additional nutrients. For simplicity, we assumed that S and K inputs in fertilizer equaled outputs; hence C_S and C_K were set equal to zero. For Ca and Mg, we accounted for inputs in manure and ag-lime and outputs in crop harvest. Manure inputs were constrained by assigning Ca:N and Mg:N values for manure and scaling Ca and Mg inputs to the manure N application rate. Ca:N and Mg:N for manure were averaged across dairy solids, swine solids, and poultry manure types (*29*). Similarly, average Ca:N and Mg:N values were assigned for crop biomass using published values for corn and soy (*30*), allowing us to approximate Ca and Mg removal in harvest.

We modeled liming rates endogenously as a function of pH. We first aligned county level liming data from 1987 (*31*) (the most recent available date) with maps of soil pH derived from NATSGO (*32*). We assigned a pH value to croplands in each county by extracting NATSGO pH values in a 10 km grid across the USA and masking out non-cropland areas using the GFSAD cropland mask (*33*). We then calculated the median cropland pH value in each county. This revealed that liming rates vary widely below pH 7, but are low above pH 7. We modeled the maximum rate of lime addition as a function of pH using a sigmoid function:

$$Lime_{max} = p_1*(1-\exp(-10^{-pH_{lab}}/p_2)^{p3}) \qquad \text{(Equation 20)}$$

Where $Lime_{max}$ was the maximum observed liming rate (t ha^{-1} y^{-1}) p_1, p_2, and p_3 were empirical constants and pH_{lab} was the laboratory-measured soil pH assumed equal to the median pH from NATSGO. We fit this function to the condition 90th percentiles of the data obtained in 0.5 pH-unit bins using the R function "nls". The parameters received estimated values of $p_1 = 0.424$, $p_2 = 1.42*10^{-7}$, and $p_3 = 1.13$.

Below the maximum liming rate, we assumed that farmers add enough lime to neutralize acidity from fertilizer and replace Ca and Mg lost in crop biomass. Consequently, the main effect of liming in the model was to maintain soil pH at the same level it would have attained under unfarmed conditions. We made this assumption because it was a reasonable compromise between two extreme alternatives: [1] assuming that farmers generally add lime aggressively to raise their soil pH to agronomically optimal levels; or [2] farmers generally do not add enough lime to maintain soil pH, and croplands are broadly acidified compared to unfarmed baseline conditions. To estimate the liming rate, we first ran the model without agricultural influence, which yielded the target pH value, pH_{target}. We then modeled lime addition as a function of pH_{lab} that increases steeply towards $Lime_{max}$ at pH_{target}:

$$Lime_{tot} = Lime_{max} * (1 - \exp(-10^{-pHlab} / 10^{-pHtarget})^{20}) \quad \text{(Equation 21)}$$

Applying this equation required approximating pH_{lab} because the model was designed to calculate the in-situ field pH, while laboratory pH was estimated as a post-processing step at some computational cost. To address this, we derived empirical linear relationships between the in-situ pH and the laboratory pH prior to running cropland simulations, with a separate relationship fitted for carbonate-buffered and carbonate free soils. These regressions explained >90% of the variation in pH_{lab} and could be used to solve Equation 21 without explicitly estimating this quantity at every model iteration, speeding up computations substantially. After applying Equation 21, we partitioned lime added into calcitic and dolomitic components. In general, crop Mg removal exceeded inputs, and so we satisfied Mg demand first. Mg demand (mol m^{-2} y^{-1}) was set equal to the cropland partial Mg budget (crop removal – manure inputs) where removal exceeded inputs and set to zero elsewhere. Dolomitic lime addition (mol m^{-2} y^{-1}) was then set to equal to Mg demand. Where Mg demand could not be met because the mass of dolomite added exceeded $Lime_{max}$, the cropland Mg budget was set equal to zero and it was assumed the Mg came from other unknown sources. Calcitic lime addition was calculated as the difference between the mass of dolomite added and $Lime_{tot}$. Ca and Mg added in lime were obtained from dolomitic and calcitic lime based on the chemical formulae for calcite and dolomite (Table S6).

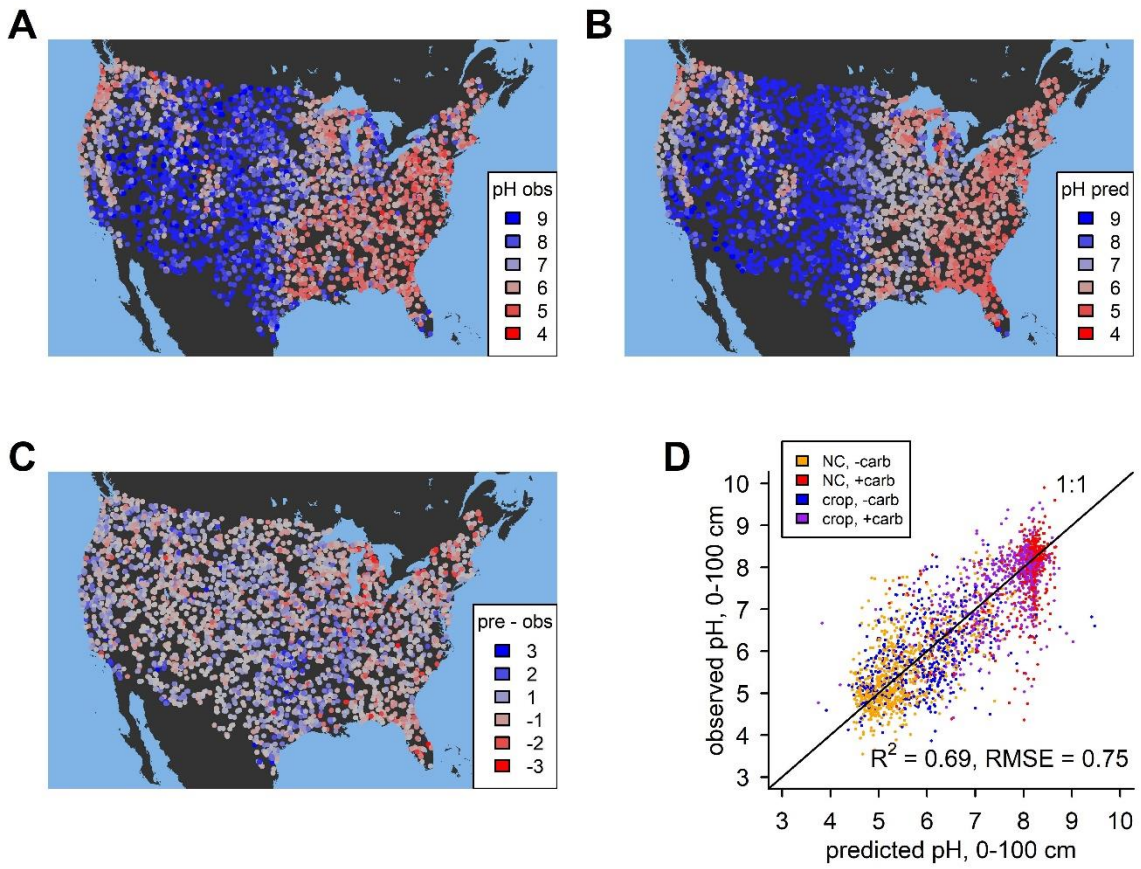

Fig. S1. Model performance matching soil pH. (A) shows observed depth-weighted average soil pH of the top 100 cm at 4,247 unique locations used for model training and validation. **(B)** shows pH simulated by the calibrated model at the same locations, and **(C)** shows the model residuals (predicted – observed pH). **(D)** shows a plot of predicted versus observed pH, with colors representing different combinations of land use and soil carbonate status (NC, -carb = non-cropland, carbonate free; NC, +carb = non-cropland, carbonates present; crop, -carb = cropland, carbonate free; crop, +carb = cropland, carbonates present). RMSE is the root mean squared error.

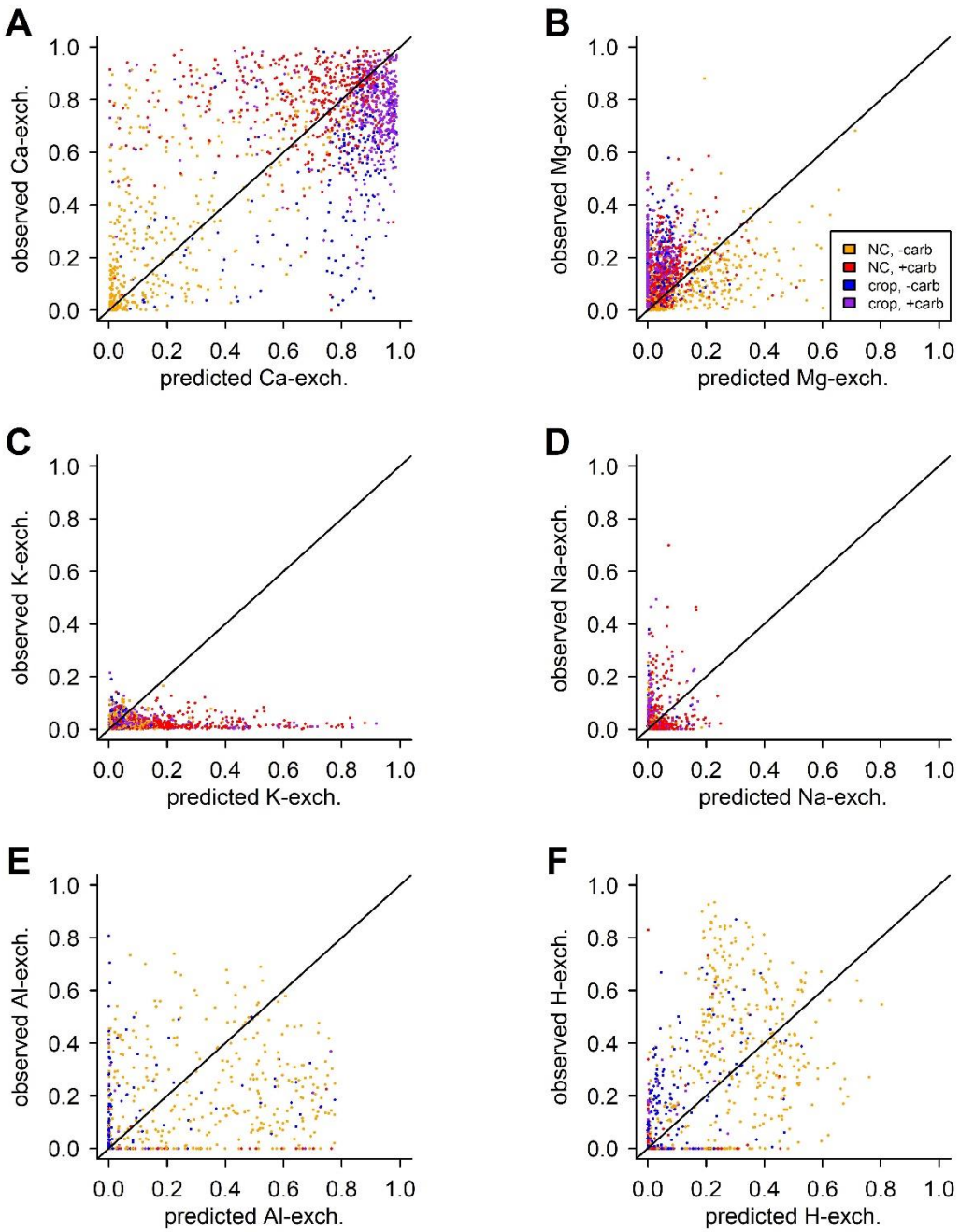

Fig. S2. Model performance for exchangeable ions. (A) – (F) show predicted versus observed exchange fractions for Ca, Mg, K, Na, Al, and H^+. Observed values represent depth-weighted averages to 100 cm taken from the NCSS database***(34)*** (n = 2,563 unique profiles). Values are normalized by total cation exchange capacity (moles cation charge / CEC). Colors represent different combinations of land use and soil carbonate status (NC, -carb = non-cropland, carbonate free; NC, +carb = non-cropland, carbonates present; crop, -carb = cropland, carbonate free; crop, +carb = cropland, carbonates present). Diagonal lines show the 1:1 relationship.

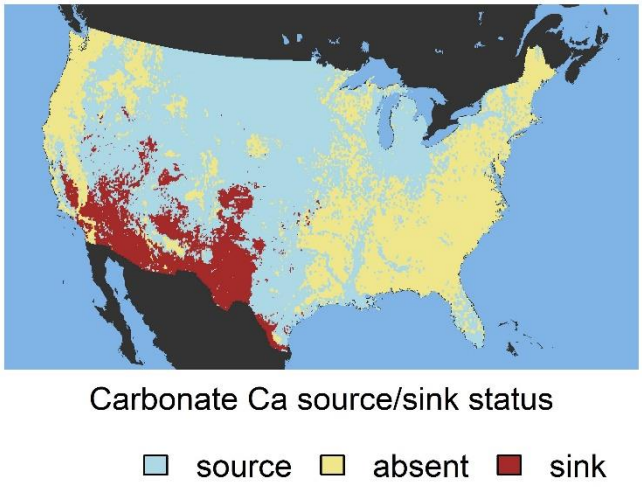

Fig. S3. Modeled carbonate source / sink status. Data show model simulations under preindustrial late Holocene conditions. Areas mapped in yellow are carbonate free, areas mapped in blue are releasing Ca via carbonate weathering, and areas mapped in red are a sink for Ca via carbonate formation.

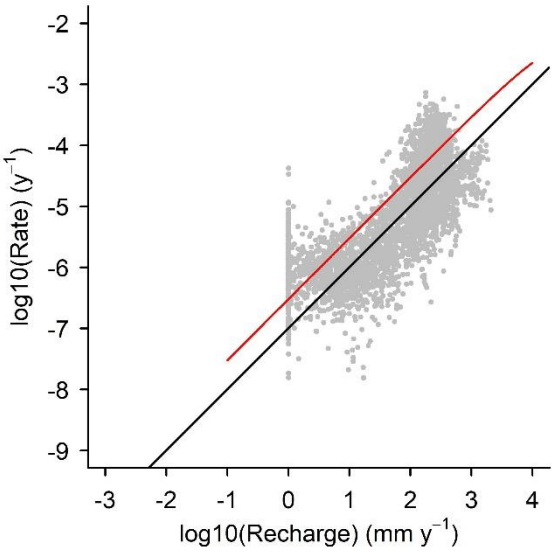

Fig. S4. Modeled plagioclase feldspar weathering rate versus recharge. Gray points show modeled feldspar weathering rates normalized by the feldspar stock versus the recharge parameter. The red line shows the non-linear fit to a compilation of field and lab weathering rates from Maher 2010 **(*3*)**, and the black line shows a fit to the same complication from Yu and Hunt 2018 **(*4*)**.

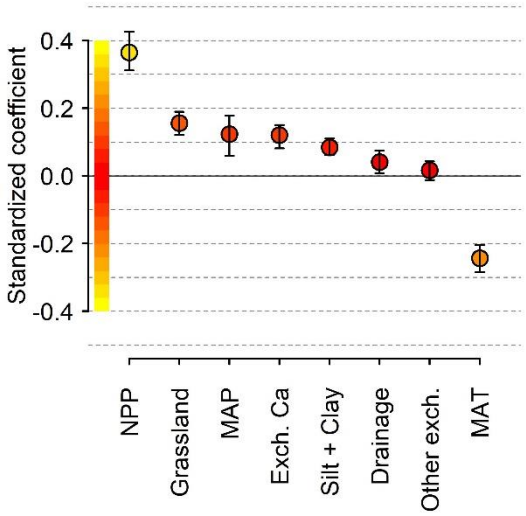

Fig. S5. Controls on A-horizon soil organic carbon stocks in the USA, with corrected CEC. Standardized regression coefficients were derived from a multivariate linear regression model, where A-horizon organic carbon stocks were predicted as a function of the eight variables listed on the horizonal axis. In this case, cation exchange capacity (CEC) was corrected for the contribution from soil organic matter prior to calculating exchangeable ion pools. In both panels, whiskers show 95% confidence intervals derived from a spatial blocked bootstrapping procedure (see Methods). The absolute value of each regression coefficient is an index of how strongly related each variable is to the response variable, and is shown with a relative color scale: yellow = maximum, red = zero. Abbreviations: NPP = net primary productivity, MAT = mean annual temperature, MAP = mean annual precipitation, Exch. Ca = total exchangeable Ca, Other exch. = sum of non-Ca exchangeable ions.

	R^2	RMSE
Ca^{2+}	0.39	0.27
Mg^{2+}	0.03	0.15
Na^{+}	0.06	0.06
K^{+}	0	0.16
Al^{3+}	0.27	0.17
H^{+}	0.45	0.16
All	0.64	0.17

Table S1. Validation statistics for exchangeable ions. R^2 values are derived by regressing observations on predictions; root mean squared error (RMSE) was calculated as the square root of the mean of the squared residuals (geochemical model predictions – observations). Statistics for all cations were obtained by treating all observed and predicted cation fractions as independent values and pooling them. Observed values represent depth-weighted averages to 100 cm taken from the NCSS database (*34*) (n = 2,563 unique profiles; 3,423 total including repeats from spatially weighted resampling). Values are normalized by total cation exchange capacity (moles cation charge / CEC).

	value	CI
intercept	-2.342	[-2.644, -2.082]
grassland	1.45	[1.205, 1.695]
base sat.	2.887	[2.433, 3.544]
silt + clay	-1.333	[-1.706, -1.004]
NPP	0.202	[-0.048, 0.451]
Drainage	0.724	[0.470, 1.039]
MAT	0.644	[0.253, 0.994]
MAP	-0.638	[-1.102, -0.162]

Table S2. Results of logistic regression analysis for Mollisol extent. Statistics are derived from a multivariate logistic regression, where the presence or absence of Mollisols was modeled as a function of potential grassland and savanna vegetation (grassland), base saturation (base sat.), soil silt + clay content, net primary productivity (NPP), USDA drainage class (drainage), Mean annual temperature (MAT), and mean annual precipitation (MAP). Continuous predictors were scaled by their standard deviations prior to fitting, whereas the binary predictor (grassland) was scaled by two times its standard deviation. Model null deviance = 136,055; Residual deviance = 97075. At a probability threshold of 0.4 the accuracy rate was 0.79; sensitivity was 0.61; and specificity was 0.86. Confidence intervals were derived from a spatially blocked bootstrapping procedure (see Methods).

	value	CI
intercept	-0.051	[-0.067, -0.036]
NPP	0.143	[0.106, 0.172]
MAP	0.152	[0.120, 0.185]
exch. Ca	0.013	[-0.014, 0.039]
grassland	-0.233	[-0.270, -0.188]
silt + clay	0.029	[-0.005, 0.062]
Drainage	0.079	[0.057, 0.103]
other exch.	0.362	[0.304, 0.421]
MAT	0.13	[0.069, 0.179]

Table S3. Results of multiple regression analysis for A-horizon SOC. Statistics are derived from a multivariate logistic regression, where log-transformed A-horizon organic carbon stocks were modeled as a function of potential grassland and savanna vegetation (grassland), exchangeable Ca (Ca exch.), non-Ca exchangeable ions (other exch.), soil silt + clay content, net primary productivity (NPP), USDA drainage class (drainage), Mean annual temperature (MAT), and mean annual precipitation (MAP). Continuous predictors were scaled by their standard deviations prior to fitting, whereas the binary predictor (grassland) was scaled by two times its standard deviation. Model $R^2 = 0.30$ and residual standard error was 0.4189. Confidence intervals were derived from a spatially blocked bootstrapping procedure (see Methods).

Ion or algebraic constraint	Equation
Ca^{2+}	$dCa/dt = D_{Ca} + A_{Ca} + C_{Ca} + R_{Cc,Ca} + R_{Do,Ca} + R_{Pl,Ca} + R_{Hb,Ca} + R_{Py,Ca} - L_{Ca}$
Mg^{2+}	$dMg/dt = D_{Mg} + A_{Mg} + C_{Mg} + R_{Do,Mg} + R_{Hb,Mg} + R_{Py,Mg} + R_{Cl,Mg} - L_{Mg}$
Na^{+}	$dNa/dt = D_{Na} + R_{Pl,Na} - L_{Na}$
K^{+}	$dK/dt = D_{K} + C_{K} + M_{K} + R_{Ks,K} + R_{Il,K} - U_{K} - L_{K}$
NO_3^{-}	$dN/dt = D_{N} + C_{N} + F_{N} - V_{N} - L_{N}$
SO_4^{2-}	$dS/dt = D_{S} + C_{S} - L_{S}$
Cl^{-}	$dCl/dt = D_{Cl} - L_{Cl}$
Charge Balance	$0 = (2[Ca^{2+}] + 2[Mg^{2+}] + [K^{+}] + [Na^{+}] + 3[Al^{3+}] + 2[Al(OH)^{2+}] + [Al(OH)_2^{+}] + 2[AlHOrg^{2+}] + [AlH_2Org^{+}] + [H^{+}]) - ([OH^{-}] + [HCO_3^{-}] + 2[CO_3^{2-}] + [H_2Org^{-}] + 2[HOrg2-] + 3[Org^{3-}] + [Al(OH)_4^{-}] + 2[SO_4^{2-}] + [NO_3^{-}] + [Cl^{-}])$
Exchange	$1 = fCa + fMg + fNa + fK + fAl + fH$

Table S4 Governing equations. Capital letters indicate rates: D = deposition (wet + dry); A = agricultural liming, C = cropland nutrient budget (inputs – uptake); R = weathering; L = leaching; F = fixation; V = volatilization. Weathering rates (mol mineral y^{-1}) were multiplied by the molar concentration of each element the mineral to yield the flux of each element from the mineral; this is indicated in the subscripts, with the mineral listed first and then the corresponding element. Minerals: Cc = calcite; Do = dolomite; Pl = plagioclase; Hb = hornblende; Py = pyroxene; Cl = chlorite; Ks = K-feldspar; Il = illite.

Parameter	Description	Value	Units	Source
Ea_{sil}	Silicate weathering activation energy	74	kJ mol^{-1} K^{-1}	(*2*)
Hr	Reference [H+] value	10^{-5}	mol l^{-1}	This study
nH	Silicate weathering reaction order for H+	0.6667	-	This study
RRPl	Relative reaction rate, plagioclase	1	-	(*1*)
RRKs	Relative reaction rate, K-feldspar	0.63	-	(*1*)
RRHb	Relative reaction rate, hornblende	0.25	-	(*1*)
RRPy	Relative reaction rate, pyroxene	1	-	This study
$log(A_{acid,Cc})$	Acid mechanism preexponential factor, calcite	-0.3	mol m^{-2} s^{-1}	(*6*)
$log(A_{neut,Cc})$	Neutral mechanism preexponential factor, calcite	-5.81	mol m^{-2} s^{-1}	(*6*)
$log(A_{CO2,Cc})$	CO_2 mechanism preexponential factor, calcite	-3.48	mol m^{-2} s^{-1}	(*6*)
$log(A_{acid,Do})$	Acid mechanism preexponential factor, dolomite	-3.19	mol m^{-2} s^{-1}	(*6*)
$log(A_{neut,Do})$	Neutral mechanism preexponential factor, dolomite	-7.53	mol m^{-2} s^{-1}	(*6*)
$log(A_{CO2,Do})$	CO_2 mechanism preexponential factor, dolomite	-5.11	mol m^{-2} s^{-1}	(*6*)
$Ea_{acid,cc}$	Acid mechanism activation energy, calcite	14.4	kJ mol^{-1} K^{-1}	(*6*)
$Ea_{neut,cc}$	Neutral mechanism activation energy, calcite	23.5	kJ mol^{-1} K^{-1}	(*6*)
$Ea_{CO2,cc}$	CO_2 mechanism activation energy, calcite	35.4	kJ mol^{-1} K^{-1}	(*6*)
$Ea_{acid,do}$	Acid mechanism activation energy, dolomite	36.1	kJ mol^{-1} K^{-1}	(*6*)
$Ea_{neut,do}$	Neutral mechanism activation energy, dolomite	52.2	kJ mol^{-1} K^{-1}	(*6*)
$Ea_{CO2,do}$	CO_2 mechanism activation energy, dolomite	34.8	kJ mol^{-1} K^{-1}	(*6*)
nH_{Cc}	Reaction order for H^+, calcite	1	-	(*6*)
$nCO_{2,Cc}$	Reaction order for CO_2, calcite	1	-	(*6*)
nH_{Do}	Reaction order for H^+, dolomite	0.5	-	(*6*)
$nCO_{2,Do}$	Reaction order for CO_2, dolomite	0.5	-	(*6*)

Table S5 Weathering rate parameters

Mineral	Abbr.	Type	Formula	Density
Plagioclase	Pl	tectosilicate	$Na_{(1-fAn)}Ca_{fAn}Al_{(1+fAn)}Si_{(3-fAn)}O_8$	$2.75f_{An} + 2.625(1-f_{An})$
K-feldspar	Ks	tectosilicate	$KAlSi_3O_8$	2.59
Pyroxene	Py	inosilicate	$MgCa(SiO_3)_2$	3.3
Hornblende	Hb	inosilicate	$Ca_2(Mg_2Fe_2Al)Si_7AlO_{22}(OH)_2$	3.1735
Chlorite	Cl	phyllosilicate	$Mg_5Al_2Si_3O_{18}H_8$	2.915
Illite	Il	phyllosilicate	$K(Al_2)(Si_3Al)O_{10}(OH)_2$	2.795
Calcite	Cc	carbonate	$CaCO_3$	2.7102
Dolomite	Do	carbonate	$CaMg(CO_3)_2$	2.85

Table S6 Mineral properties. f_{An} = anorthite molar fraction. Densities are midpoints of reported ranges from Mindat.org.

Reaction	ΔS (kJ K^{-1} mol^{-1})	ΔH (kJ mol^{-1})	logK	source
$CO_{2\ (g)} \leftrightarrow CO_{2\ (aq)}$	-0.09616924	-20.28821600		(*8*, *9*)
$CO_{2\ (aq)} + H_2O \leftrightarrow HCO_3^- + H^+$	-0.08904506	9.70167230		(*8*, *9*)
$HCO_3^- \leftrightarrow CO_3^{2-} + H^+$	-0.14844832	14.69839200		(*8*, *9*)
$H_2O \leftrightarrow OH^- + H^+$	-0.08063522	55.81353630		(*8*, *9*)
$Al(OH)_{3\ (s)} \leftrightarrow Al(OH)_{3\ (aq)}$	-0.00908996	50.45803923		(*8*, *9*)
$Al(OH)_{3\ (aq)} + 3H^+ \leftrightarrow Al^{3+} + 3H_2O$	-0.18933085	-153.61153602		(*8*, *9*)
$Al(OH)_{3\ (aq)} + 2H^+ \leftrightarrow Al(OH)_2^+ + 2H_2O$	-0.10062704	-98.86893231		(*8*, *9*)
$Al(OH)_{3\ (aq)} + 1H^+ \leftrightarrow Al(OH)^{2+} + H_2O$	-0.01697332	-39.97106033		(*8*, *9*)
$Al(OH)_{3\ (aq)} + H_2O \leftrightarrow Al(OH)_4^- + H^+$	-0.02572859	25.43199965		(*8*, *9*)
$CaCO_{3\ (s)} \leftrightarrow Ca^{2+} + CO_3^{2-}$	-0.19820780	-11.49904000		(*8*, *9*)
$CaMgC_2O_{6\ (s)} \leftrightarrow Ca^{2+} + Mg^{2+} + 2CO_3^{2-}$	-0.44944386	-34.26448628		(*8*, *9*)
$Mg_5Al_2Si_3O_{18}H_{8\ (s)} + 10H^+ \leftrightarrow 2Al(OH)_{3\ (aq)} + 5Mg^{2+} + 3H_4SiO_{4\ (aq)}$	-0.08814278	-56.42611		(*8*, *9*)
$KAl_3Si_3O_{12}H_{2\ (s)} + H^+ + 9H_2O \leftrightarrow 3Al(OH)_{3\ (aq)} + K^+ + 3H_4SiO_{4\ (aq)}$	-0.0772809	199.2072		(*8*, *9*)
SiO_2(amorph) + $2H_2O \leftrightarrow H_4SiO_4$	-0.01114692	10.56612		(*8*, *9*)
$H_3Org \leftrightarrow H_2Org^- + H^+$			-2.653	(*14*)
$H_2Org^- \leftrightarrow HOrg^{2-} + H^+$			-6.233	(*14*)
$HOrg^{2-} \leftrightarrow Org^{3-} + H^+$			-7.467	(*14*)
$AlH_2Org^{2+} \leftrightarrow H^+ + AlHOrg^+$			-4.963	(*14*)
$AlHOrg^+ \leftrightarrow H^+ + AlOrg$			-4.040	(*14*)
$AlOrg \leftrightarrow Al^{3+} + Org^{3-}$			-10.020	(*14*)
$3Ca\text{-}X + 2Al^{3+} \leftrightarrow 2Al\text{-}X + 3Ca^{2+}$			2.026 (s); 1.195 (lo); 0.106 (cl)	(*16*)
$3Mg\text{-}X + 2Al^{3+} \leftrightarrow 2Al\text{-}X + 3Mg^{2+}$			2.811 (s); 1.244 (lo); 0.599 (cl)	(*16*)
$3Na\text{-}X + Al^{3+} \leftrightarrow Al\text{-}X + 3Na^+$			1.811 (s); 0.646 (lo); 1.045 (cl)	(*16*)
$3K\text{-}X + Al^{3+} \leftrightarrow Al\text{-}X + 3K^+$			-0.917 (s); -2.413 (lo); -3.561 (cl)	(*16*)
$3H\text{-}X + Al^{3+} \leftrightarrow Al\text{-}X + 3H^+$			-6.924 (s); -7.532 (lo); -9.923 (cl)	(*16*)

Table S7 Equilibrium reactions and thermodynamic parameters. For exchange reactions logK values are for sand, loess, and clay respectively based on (*16*).

References

1. A. F. White, H. L. Buss, "Natural Weathering Rates of Silicate Minerals" in *Treatise on Geochemistry* (Elsevier, 2014; https://linkinghub.elsevier.com/retrieve/pii/B9780080959757005040), pp. 115–155.

2. A. West, A. Galy, M. Bickle, Tectonic and climatic controls on silicate weathering. *Earth and Planetary Science Letters* **235**, 211–228 (2005).

3. K. Maher, The dependence of chemical weathering rates on fluid residence time. *Earth and Planetary Science Letters* **294**, 101–110 (2010).

4. F. Yu, A. G. Hunt, Predicting soil formation on the basis of transport-limited chemical weathering. *Geomorphology* **301**, 21–27 (2018).

5. E. W. Slessarev, Y. Lin, N. L. Bingham, J. E. Johnson, Y. Dai, J. P. Schimel, O. A. Chadwick, Water balance creates a threshold in soil pH at the global scale. *Nature* **540**, 567–569 (2016).

6. Palandri, Y. Kharaka, A compilation of rate parameters of water-mineral interaction kinetics for application to geochemical modeling (2004).

7. N. G. Swoboda-Colberg, J. I. Drever, Mineral dissolution rates in plot-scale field and laboratory experiments. *Chemical Geology* **105**, 51–69 (1993).

8. J. W. Johnson, E. H. Oelkers, H. C. Helgeson, SUPCRT92: A software package for calculating the standard molal thermodynamic properties of minerals, gases, aqueous species, and reactions from 1 to 5000 bar and 0 to 1000°C. *Computers & Geosciences* **18**, 899–947 (1992).

9. J. M. Dick, CHNOSZ: Thermodynamic Calculations and Diagrams for Geochemistry. *Front. Earth Sci.* **7**, 180 (2019).

10. J. Gaillardet, D. Calmels, G. Romero-Mujalli, E. Zakharova, J. Hartmann, Global climate control on carbonate weathering intensity. *Chemical Geology* **527**, 118762 (2019).

11. X. Lan, R. Keeling, Trends in atmospheric carbon dioxide. https://gml.noaa.gov/ccgg/trends/data.html.

12. D. M. Etheridge, L. P. Steele, R. L. Langenfelds, R. J. Francey, J. -M. Barnola, V. I. Morgan, Natural and anthropogenic changes in atmospheric CO_2 over the last 1000 years from air in Antarctic ice and firn. *J. Geophys. Res.* **101**, 4115–4128 (1996).

13. J. W. Raich, W. H. Schlesinger, The global carbon dioxide flux in soil respiration and its relationship to vegetation and climate. *Tellus B* **44**, 81–99 (1992).

14. H. Fakhraei, C. T. Driscoll, Proton and Aluminum Binding Properties of Organic Acids in Surface Waters of the Northeastern U.S. *Environ. Sci. Technol.* **49**, 2939–2947 (2015).

15. M. Camino-Serrano, B. Guenet, S. Luyssaert, P. Ciais, V. Bastrikov, B. De Vos, B. Gielen, G. Gleixner, A. Jornet-Puig, K. Kaiser, D. Kothawala, R. Lauerwald, J. Peñuelas, M. Schrumpf, S. Vicca, N. Vuichard, D. Walmsley, I. A. Janssens, ORCHIDEE-SOM:

modeling soil organic carbon (SOC) and dissolved organic carbon (DOC) dynamics along vertical soil profiles in Europe. *Geosci. Model Dev.* **11**, 937–957 (2018).

16. W. Vries, M. Posch, Derivation of cation exchange constants for sand, loess, clay and peat soils on the basis of field measurements in the Netherlands (2003). https://library.wur.nl/WebQuery/wurpubs/349403.

17. Y. Kanzaki, I. Chiaravalloti, S. Zhang, N. J. Planavsky, C. T. Reinhard, In silico calculation of soil pH by SCEPTER v1.0. *Geosci. Model Dev.* **17**, 4515–4532 (2024).

18. M. Posch, G. J. Reinds, A very simple dynamic soil acidification model for scenario analyses and target load calculations. *Environmental Modelling & Software* **24**, 329–340 (2009).

19. W. R. Wieder, C. C. Cleveland, D. M. Lawrence, G. B. Bonan, Effects of model structural uncertainty on carbon cycle projections: biological nitrogen fixation as a case study. *Environ. Res. Lett.* **10**, 044016 (2015).

20. A. S. Wymore, P. J. Johnes, S. Bernal, E. N. J. Brookshire, H. M. Fazekas, A. M. Helton, A. Argerich, R. T. Barnes, A. A. Coble, W. K. Dodds, S. Haq, S. L. Johnson, J. B. Jones, S. S. Kaushal, P. Kortelainen, C. López-Lloreda, B. M. Rodríguez-Cardona, R. G. M. Spencer, P. L. Sullivan, C. A. Yates, W. H. McDowell, Gradients of Anthropogenic Nutrient Enrichment Alter N Composition and DOM Stoichiometry in Freshwater Ecosystems. *Global Biogeochemical Cycles* **35**, e2021GB006953 (2021).

21. D. P. Swaney, R. W. Howarth, B. Hong, Nitrogen use efficiency and crop production: Patterns of regional variation in the United States, 1987–2012. *Science of The Total Environment* **635** (2018).

22. V. Smil, Nitrogen in crop production: An account of global flows. *Global Biogeochemical Cycles* **13**, 647–662 (1999).

23. R. L. Kellogg, C. H. Lander, D. C. Moffitt, N. Gollehon, Manure nutrients relative to the capacity of cropland and pastureland to assimilate nutrients: Spatial and temporal trends for the United States (2000).

24. G. L. Velthof, D. Oudendag, H. P. Witzke, W. A. H. Asman, Z. Klimont, O. Oenema, Integrated Assessment of Nitrogen Losses from Agriculture in EU-27 using MITERRA-EUROPE. *J of Env Quality* **38**, 402–417 (2009).

25. G. W. Roth, R. H. Fox, Soil Nitrate Accumulations following Nitrogen-Fertilized Corn in Pennsylvania. *J of Env Quality* **19**, 243–248 (1990).

26. N. Ziadi, G. Bélanger, A. Claessens, Relationship between soil nitrate accumulation and in-season corn N nutrition indicators. *Can. J. Plant Sci.* **92**, 331–339 (2012).

27. Xu-Ri, I. C. Prentice, Terrestrial nitrogen cycle simulation with a dynamic global vegetation model. *Global Change Biology* **14**, 1745–1764 (2008).

28. T. O. West, V. Bandaru, C. C. Brandt, A. E. Schuh, S. M. Ogle, Regional uptake and release of crop carbon in the United States. *Biogeosciences* **8**, 2037–2046 (2011).

29. "Animal Manure Production and Utilization in the US" in *Applied Manure and Nutrient Chemistry for Sustainable Agriculture and Environment* (Springer Netherlands, Dordrecht, 2014; https://link.springer.com/10.1007/978-94-017-8807-6_1), pp. 1–21.

30. M. D. Masters, C. K. Black, I. B. Kantola, K. P. Woli, T. Voigt, M. B. David, E. H. DeLucia, Soil nutrient removal by four potential bioenergy crops: Zea mays, Panicum virgatum, Miscanthus×giganteus, and prairie. *Agriculture, Ecosystems & Environment* **216**, 51–60 (2016).

31. M. Haines, P. Fishback, P. Rhode, United States Agriculture Data, 1840 - 2012: Version 4, version v4, ICPSR - Interuniversity Consortium for Political and Social Research (2014); https://doi.org/10.3886/ICPSR35206.V4.

32. Soil Survey Staff, Gridded National Soil Survey Geographic (gNATSGO) Database for the Conterminous United States.

33. P. Teluguntla, P. Thenkabail, J. Xiong, M. Gumma, C. Giri, C. Milesi, M. Ozdogan, R. Congalton, J. Tilton, T. Sankey, R. Massey, A. Phalke, K. Yadav, NASA Making Earth System Data Records for Use in Research Environments (MEaSUREs) Global Food Security Support Analysis Data (GFSAD) Crop Mask 2010 Global 1 km V001, NASA Land Processes Distributed Active Archive Center (2016); https://doi.org/10.5067/MEASURES/GFSAD/GFSAD1KCM.001.

34. National Cooperative Soil Survey, National Cooperative Soil Survey Soil Characterization Database (2018). http://ncsslabdatamart.sc.egov.usda.gov/.